American Mineralogist, Volume 89, pages 132–146, 2004

Vibrational spectroscopy of pyrope-majorite garnets: Structural implications

A.M. HOFMEISTER,[1,*] P.A. GIESTING,[1,†] B. WOPENKA,[1] G.D. GWANMESIA,[2] AND B.L. JOLLIFF[1]

[1]Department of Earth and Planetary Science, Washington University, St. Louis, Missouri 63130, U.S.A.
[2]Department of Physics and Pre-engineering, Delaware State University, Dover, Delaware 19901, U.S.A.

ABSTRACT

Infrared reflectance, thin-film absorbance, and polarized Raman spectra were acquired from ~100 to ~4000 cm^{-1} from polycrystalline garnets along the pyrope (Py = $Mg_3Al_2Si_3O_{12}$)-majorite [Mj = $Mg_3(MgSi)Si_3O_{12}$] join. We measured Py_{100}, Mj_{39}, Mj_{45}, Mj_{80}, and natural single-crystal, nearly end-member pyrope. Consistency is obtained between measured absorption spectra and absorption coefficients calculated through Kramers-Kronig analysis of reflectivity (*R*) data, if *R*-values are scaled to account for losses through scattering. The widths of the lattice modes double from each end-member toward the middle of the binary, whereas frequencies are nearly independent of composition. Strong polarization of Raman peaks of all our samples except pyrope shows that the space group is reduced from cubic, even for the Al-rich majorites. The largest number of IR or Raman peaks is observed for Mj_{80}. The number of peaks for Al-rich majorites lies between those seen for cubic pyrope and $I4_1/a$ majorite. The behavior of symmetry-breaking modes supports the $I4_1/acd$ space group, which was inferred from X-ray data for Mj contents near 30 to 45% (Nakatsuka et al. 1999a). Also, the internal mode types that are expected for isolated SiO_4 tetrahedra in any garnet-like structure do not fully describe the patterns of peaks seen for some intermediate compositions along the Py-Mj join. The appearance of Si_{oct}-O-Si_{tet} bending modes in the available spectral data for Mj contents near 30–40 and 80–90%, but not near 45–50%, is attributed to two-mode behavior. Specifically, disruption of the structural chain -Si_{oct}-O-Si_{tet}-O-Si_{oct}-O-Si_{tet}- in Si-rich majorites by units such as $-Si_{oct}-O-Si_{tet}\begin{cases}-O-Al\\-O-Mg\\-O-Al\end{cases}$ alters the electrostatic balance so that the internal modes are not entirely described by motions of isolated SiO_4 tetrahedra. Short chains are formed at both high and low Al contents, promoting coupling of Si octahedral and tetrahedral vibrations. Near Mj_{50}, each tetrahedron is linked (on average) to four octahedra containing two Al-, one Si-, and one Mg, and the Si_{oct}-O-Si_{tet} bending modes disappear. Order-disorder in majorite garnets is characterized not only by increased peak widths, but also by the presence of modes due to the bridging O atoms, whereas splittings and the appearance of new peaks indicate the space group for non-cubic garnets.

INTRODUCTION

High-pressure petrological studies indicate that majorite-rich garnet [$4MgSiO_3 = Mg_3(MgSi)Si_3O_{12}$] dominates the transition zone of the Earth's mantle, from 400–700 km (e.g., Ringwood and Major 1966; Akaogi and Akimoto 1977; Kanzaki 1987; Gasparik 1989, 1990). Depending on the petrological model, estimates of the garnet component in this region ranges from 40–70% by volume of the mineral assemblage (e.g., Bass and Anderson 1984; Irifune and Ringwood 1987; Vacher et al. 1998; Weidner and Wang 2000; Hirose et al. 2001). The volumetric importance of this phase is largely due to the ease with which the garnet structure incorporates diverse cations.

Previous IR data on the lattice modes of majoritic garnet have been limited to frequencies above 400 cm^{-1} and to $MgSiO_3$ and Al-rich majorites, and were obtained from dispersions of powder in KBr pellets (Jeanloz 1981; Kato and Kumazawa 1985; McMillan et al. 1989), which tend to have artifacts (e.g., Horak and Vitek 1978; Hofmeister 1995). Previous Raman measurements of lattice modes are available across the binary (McMillan et al. 1989; Rauch et al. 1996; Manghnani et al. 1998; Chopelas 1999), but polarized studies were not attempted, and for a given composition, available spectra differ significantly.

The present study uses infrared (IR) and Raman techniques over wide frequency ranges, including some polarization measurements, to characterize lattice modes of binary majorite-pyrope garnets. One companion paper (Giesting et al. 2004) calculates thermal conductivity, entropy, and heat capacity across the majorite-pyrope binary, based on the results presented here. A second companion paper (Giesting et al. in preparation) describes the impurities (hydroxyl, water, hydrocarbons, disordered graphite, and Cr^{3+}) present as trace to minor amounts in our samples. The spectroscopic features of these impurities are mentioned in the present paper only when they are superimposed on the lattice modes.

STRUCTURE, SYMMETRY, AND POSSIBLE TWO-MODE BEHAVIOR OF MAJORITES

Pyrope has the cubic space group $Ia\bar{3}d$. The modes for cubic garnet are summarized in the footnotes to Table 1. For a full

* E-mail:hofmeist@levee.wustl.edu
† Present address: Department of Civil Engineering and Geological Sciences, The University of Notre Dame, Notre Dame, Indiana 46556, U.S.A.

TABLE 1. Symmetry analysis of $I4_1/acd$ garnet (D_{4h}^{20} with 240 total vibrations)

Atom	Site	Symmetry	Raman A_{1g}	A_{2g}	Raman B_{1g}	Raman B_{2g}	Raman E_g	— A_{1u}	IR A_{2u}	— B_{1u}	— B_{2u}	IR E_u
Mg^{2+}	8b	$D_2''(4)$	0	1	1	0	2	0	1	1	0	2
	16e	$C_2'(8)$	1	2	1	2	3	1	2	1	2	3
Mg,Si	16c	$C_i(8)$	0	0	0	0	0	3	3	3	3	6
Si^{4+}	8a	$S_4(4)$	0	0	1	1	2	1	1	0	0	2
	16e	$C_2'(8)$	1	2	1	2	3	1	2	1	2	3
O^{2-}	3x32g	3x $C_1(16)$	9	9	9	9	18	9	9	9	9	18
Total ‡			11	14	13	14	28	15	18*	15	16	34*
SiO_4 †			$2\upsilon_1$	υ_1	υ_1		υ_1	υ_1		$2\upsilon_1$	υ_1	υ_1
			$3\upsilon_2$	υ_2	$3\upsilon_2$	υ_2	$2\upsilon_2$	$3\upsilon_2$	υ_2	$3\upsilon_2$	υ_2	$2\upsilon_2$
			υ_3	$2\upsilon_3$	$2\upsilon_3$	$3\upsilon_3$	$5\upsilon_3$	$2\upsilon_3$	$3\upsilon_3$	υ_3	$2\upsilon_3$	$5\upsilon_3$
			υ_4	$2\upsilon_4$	$2\upsilon_4$	$3\upsilon_4$	$5\upsilon_4$	$2\upsilon_4$	$3\upsilon_4$	υ_4	$2\upsilon_4$	$5\upsilon_4$
$R(SiO_4)$			2	3	2	2	5	1	2	2	3	5
$T(SiO_4)$			1	2	1	3	5	2	3*	1	2	5*
T(oct)			0	0	0	0	0	3	3	3	3	6
T(dod)			1	3	2	2	5	1	3	2	2	5

Notes: R = rotation/libration; T = translation; υ_1 = symmetric stretching; υ_2 = symmetric bending; υ_3 = asymmetric stretching; and υ_4 = asymmetric bending. This breakdown into internal and external modes presumes the SiO_4 tetrahedron vibrates as if isolated.

* For each of these symmetries, the total includes one acoustic mode.

† For intermediate compositions local modes can exist: υ_1 becomes a more complicated Si-O stretching motion, and υ_2 becomes a bending motion involving Si_{oct}-O-Si_{tet}, see text.

‡ The total modes of cubic garnet (O_h^{10}) are $3A_{1g} + 5A_{2g} + 8E_g + 14T_{1g} + 14T_{2g} + 5A_{1u} + 5A_{2u} + 10E_u + 18T_{1u} + 16T_{2u}$. Correlations are: $A_{1g} + E_g \rightarrow A_{1g}$(tetrag.); $T_{1g} \rightarrow A_{2g}$(tetrag.); $A_{2g} + E_g \rightarrow B_{1g}$(tetrag.); $T_{2g} \rightarrow B_{2g}$(tetrag.); $T_{1g} + T_{2g} \rightarrow E_g$(tetrag.); $A_{1u} + E_u \rightarrow A_{1u}$(tetrag.); $T_{1u} \rightarrow A_{2u}$(tetrag.); $A_{2u} + E_u \rightarrow B_{1u}$(tetrag.); $T_{2u} \rightarrow B_{2u}$(tetrag.); $T_{1u} + T_{2u} \rightarrow E_u$(tetrag.)

symmetry analysis (after Fateley et al. 1972) see Hofmeister and Chopelas (1991). A complete solid solution exists between pyrope and majorite. The cubic garnet structure is known to exist at very low Mj contents (e.g., Nakatsuka et al. 1999a); the question is, how much Si can be incorporated without modification of this structure?

For majorite-pyropes with more than ~75 mol% $MgSiO_3$, the structure is tetragonal, $I4_1/a$, due to ordering of Si and Mg at the octahedral site (Kato and Kumazawa 1985; Sawamoto 1987; Angel et al. 1989; Heinemann et al. 1997). For $MgSiO_{-3,}$ cation disorder ranges from partial (Angel et al. 1989) to almost complete (Phillips et al. 1992); yet, all samples are metrically tetragonal (the lattice constant $a \neq c$). Orthorhombic symmetry for Mj_{93} at ambient conditions was proposed based on changes in the Raman spectra with pressure (Rauch et al. 1996).

Crystallographic refinements of garnets with Mj contents ranging from ~10 to 64 mol% reveal a discontinuity in the dependence of pseudo-cubic volume on Mj content near Mj_{30}, indicating a phase transition (Nakatsuka et al. 1999a). The space group of Al-rich majorites is most probably $I4_1/acd$, which is the maximal subgroup of the cubic parent structure (Nakatsuka et al. 1999a). Although this study may have shortcomings in its methodology (P. Burns, pers. comm. 2003), the basic result (a phase transition to the lower symmetry space group at low Mj contents) is corroborated by the vibrational spectroscopic data in this paper.

Tables 1 and 2 provide complete symmetry analyses of both tetragonal derivatives of the garnet structure. An incomplete symmetry analysis of $I4_1/a$ was given by McMillan et al. (1989). The lower sections of Tables 1 and 2 enumerate the internal modes of the Si tetrahedra and external modes, assuming that the Si tetrahedra in majorite vibrate as if isolated.

If one-mode behavior (e.g., Chang and Mitra 1968) predominates, i.e., frequencies change linearly across the series, then the spectra expected for any derivative structure can be deduced from symmetry considerations. Reduction of symmetry from space group $Ia\bar{3}d$ to $I4_1/acd$ requires that the triply degenerate (T_{1u}) IR-active modes of cubic garnets exist in both the A_{2u} and E_u symmetries, and that the E_u symmetry has additional modes arising from the folding of inactive modes of the parent structure. These "symmetry breaking" modes are the same set as those listed under B_{2u} in Table 1, and should be readily observed in the IR spectra of ordered garnets. Reduction of symmetry from $Ia\bar{3}d$ to $I4_1/a$ causes the triply degenerate IR-active modes of cubic garnets to be similarly split between the A_u and E_u symmetries, but for this case, both E_u and A_u have additional modes. The stronger, doubly degenerate E_u symmetry should dominate an unpolarized IR spectrum of tetragonal garnet, providing not only the internal modes for the SiO_4 tetrahedron that are expected for cubic garnets, but the additional modes υ_1, υ_2, $2\upsilon_3$, and $2\upsilon_4$ (see Table 1). The weaker A_u modes probably would not be distinct except for two υ_2-type modes that are not present in E_u (Table 2). The translations and rotation-librations behave similarly, but

TABLE 2. Symmetry analysis of $I4_1/a$ garnet (C_{4h}^6 with 240 total vibrations)

Atom	Site	Symmetry	Raman A_g	B_g	E_g	IR A_u	— B_u	IR E_u
Mg^{2+}	8f	$C_1(8)$	3	3	3	3	3	3
	4e	$C_2(4)$	1	1	2	1	1	2
	4c	$C_i(4)$	0	0	0	3	3	3
Si^{4+}	4d	Ci(4)	0	0	0	3	3	3
	2a	$S_4(2)$	0	1	1	1	0	1
	2b	$S_4(2)$	0	1	1	1	0	1
	8f	$C_1(8)$	3	3	3	3	3	3
O^{2-}	48f	6x $C_1(8)$	18	18	18	18	18	18
Total‡			25	27	28	33*	31	34*
Internal			$3\upsilon_1$	υ_1	υ_1	υ_1	$3\upsilon_1$	υ_1
SiO_4†			$4\upsilon_2$	$4\upsilon_2$	$4\upsilon_2$	$4\upsilon_2$	$4\upsilon_2$	$2\upsilon_2$
			$3\upsilon_3$	$5\upsilon_3$	$5\upsilon_3$	$5\upsilon_3$	$3\upsilon_3$	$5\upsilon_3$
			$3\upsilon_4$	$5\upsilon_4$	$5\upsilon_4$	$5\upsilon_4$	$3\upsilon_4$	$5\upsilon_4$
$R(SiO_4)$			5	3	5	3	5	5
$T(SiO_4)$			3	5	5	5*	3	5*
T(Si, oct)			0	0	0	3	3	3
T(Mg, oct)			0	0	0	3	3	3
T(Mg, dod)			4	4	5	4	4	5

Notes: See Table 1.

Correlations with cubic garnet are: $A_{1g} + E_g + T_{1g} \rightarrow A_g$; $A_{2g} + E_g + T_{2g} \rightarrow B_g$; $T_{1g} + T_{2g} \rightarrow E_g$; $A_{1u} + E_u + T_{1u} \rightarrow A_u$; $A_{2u} + E_u + T_{2u} \rightarrow B_u$; $T_{1u} + T_{2u} \rightarrow E_u$.

Correlations with D_{4h}^{20} are: $A_{1g} + A_{2g} \rightarrow A_g$; $B_{1g} + B_{2g} \rightarrow B_g$; $E_g \rightarrow E_g$; $A_{1u} + A_{2u} \rightarrow A_u$; $B_{1u} + B_{2u} \rightarrow B_u$; $E_u \rightarrow E_u$.

because these types (T and R) occur at lower frequency, the correlations may be more difficult to decipher.

The Raman-active modes should follow similar patterns (Tables 1 and 2). However, the Raman modes differ significantly in that A-type bands are strong, and should dominate an unpolarized spectrum, as is the case for pyrope and other cubic garnets (Hofmeister and Chopelas 1991; Kolesov and Geiger 1998, 2000). Thus, for $I4_1/acd$ garnets, the unpolarized spectrum will contain the A_{1g} and E_g modes present in the cubic phase (plus the strongest T_{1g} modes from cubic garnet), whereas for the $I4_1/a$, garnets, the unpolarized spectrum should consist of all the modes that are active in cubic garnets (A_{1g}, E_g, and T_{1g}), plus the strongest modes arising from the inactive symmetries A_{2g} and B_{2g}.

Several of the other space groups suggested by ordering schemes (Hatch and Griffin 1989) have symmetry breaking patterns that cause all the modes in cubic garnet to appear in the A-type symmetry. Symmetry analyses of some of these structures are found in the appendix of McAloon and Hofmeister (1993). Because the results from the present study are consistent with the tetragonal space groups and no clear evidence exists for the large number of modes expected for the orthorhombic and lower symmetries (e.g., *Fddd* has 98 IR-active modes), these lower symmetry structures are not covered in detail. However, two space groups with higher symmetries may be relevant. For $R\bar{3}$bar (C_{3i}^2), the correlations of the gerade (g) modes with cubic garnet are: $A_{1g} + A_{2g} + T_{1g} + T_{2g} \rightarrow A_g$; $A_{1g} + A_{2g} + E_g + T_{1g} + T_{2g} \rightarrow E_g$ and likewise for the u (ungerade) modes. For $R\bar{3}c$ (D_{3d}^6), the correlations are: $A_{1g} + F_{2g} + \rightarrow A_{1g}$ (hex.); $A_{2g} + F_{1g} + \rightarrow A_{2g}$ (hex.); and $E_g + T_{1g} + T_{2g} \rightarrow E_g$ (hex.), and likewise for the ungerade modes. The space group $I4_1/a$ can be distinguished from these and all the other possible space groups by the E_g modes of cubic garnet being strong in unpolarized data through the correlation $A_{1g} + E_g \rightarrow A_{1g}$ (tetrag.).

Two-mode behavior gives rise to additional (local) modes for solid solutions that are not due to symmetry reduction, but rather to mass or bonding differences (Chang and Mitra 1968; see McAloon and Hofmeister 1995; Hofmeister et al. 1996 for garnets in specific). Solid solutions of majorite and pyrope possess modes at frequencies near 700 cm^{-1} that suggest the possible existence of Si-O-Si bending motions (Rauch et al. 1996). Similar peak positions exist in chain silicates. Jeanloz (1981) and McMillan et al. (1989) considered involvement of octahedral Si as the origin of the modes near 700 cm^{-1}. However, because the octahedral cation is stationary in the gerade symmetries (Tables 1 and 2), and because modes near 700 cm^{-1} are present in Raman spectra (Rauch et al. 1996), assignment to octahedral stretching motions is questionable, although a bending motion (Si_{oct}-O-Si_{tet}) is possible. Bonding of this unit is strengthened when the octahedral cations corner-linked to the tetrahedron are not all Si,

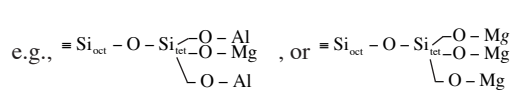

near the majorite end-member. Because all of the O atoms bonded to the octahedrally coordinated Si atom involve apices of Si tetrahedra, it is only the constitution of the octahedra surrounding any given tetrahedron that affects the bending motions about Si_{tet}. The above units can be considered as short chains. In these truncated chains, the symmetric stretch and bends (υ_1 and υ_2) of SiO_4, but not the asymmetric bends and stretches, would be affected by stronger bonding to the octahedra. The υ_1 stretch of the isolated tetrahedra becomes a combined breathing motion of the tetrahedra and octahedra, and the υ_2 bend pivots about the (stationary) octahedral Si. For simplicity, we describe these two modes as Si_{tet}-Si_{oct} and Si_{oct}-O-Si_{tet} vibrations, and refer to the phenomena as octahedral-tetrahedral coupling. As a change of bonding can produce two-mode behavior (Chang and Mitra, 1968), Si_{tet}-Si_{oct} and Si_{oct}-O-Si_{tet} could appear for intermediate compositions, with intensities proportional to the number of truncated chains. The intensities of the υ_1 and υ_2 modes of the isolated tetrahedra would be correspondingly reduced. However, compositions at the middle of the binary present a special case: all tetrahedral Si should have, on average, as second nearest neighbors one Mg, one Si, and two Al atoms to locally balance charge through Pauling's rules, which, over a slightly larger distance, averages out any imbalances in bonding. For the ordered majorite end-member, all tetrahedral sites are surrounded by octahedra containing 2Si and 2Mg. Because of this balance, the tetrahedra in majorite vibrate as if isolated, which is the case in crustal garnets. If Si_{tet}-Si_{oct} stretches and Si_{oct}-O-Si_{tet} bends exist as local modes, their intensities should be greatest near 25 and 75 mol% majorite.

It is also possible that few of the tetrahedra vibrate as if they are isolated near Mj contents of 25 and 75%. In this case, the division into internal and external modes is unlike that of pyrope, and inferring the space group from vibrational spectra would require a complete set of polarized data to count all modes in all symmetries.

SYNTHESES PROCEDURES

The specimens used in this study are nearly homogeneous polycrystalline pyrope-majorite garnets, which were originally prepared for ultrasonic studies. The starting material for each hot-pressing experiment was very fine-grained powder ground from a homogeneous glass of the selected composition. All glass starting material was ground in an agate mortar under alcohol to very fine powder of 2–5 micrometers and then dried in an oven at 170 °C for 5 h (see Gwanmesia et al. 2000). The powder was packed in a Pt capsule, cold-sealed and inserted into the appropriate cell assembly of a 2000 ton uniaxial split-sphere apparatus (USSA-2000).

The hot-pressing procedure is described by Gwanmesia et al. (1990; also see Gwanmesia and Liebermann 1992; Gwanmesia et al. 1993). The Py_{100} sample was synthesized in a cell assembly utilizing graphite as heater, while $LaCrO_3$ was used as heater for the syntheses of Mj_{39}, Mj_{45}, and Mj_{80} as described by Gwanmesia and Liebermann (1992) and Gwanmesia et al. (1993). Details of the pressure-temperature-time (*P-T-t*) path used to fabricate all specimens are in Gwanmesia et al. (2000). Our Py_{100} was synthesized at 5 GPa and 1350 °C, Mj_{39} at 18 GPa and 1200 °C, and Mj_{45} and Mj_{80} at 18.5 GPa and 1850 °C. For each experiment, the sample was maintained at the peak *P* and *T* condition for 2 h. The hot-pressing *P-T-t* path also involves an annealing period (8–16 h) during which the sample temperature is maintained at 600–700 °C while the pressure is slowly reduced (see Gwanmesia et al. 2000).

Sample descriptions and chemical compositions

The end-product polycrystalline disks, measuring about 2 mm in diameter, were mounted in brass rings, using "Crystal Bond" epoxy. The Py_{100} sample is opaque black, Mj_{39} is opaque white, Mj_{45} is translucent white, and Mj_{80} is semi-translucent and light gray. These polycrystalline samples took an indifferent polish, attributed to plucking of small grains from the surface. Individual grains from highly reflective spots on the surfaces were probed during acquisition of Raman spectra, and many grains were used for thin-film IR measurements, whereas most of the surface of the cylindrical samples was examined using IR reflectivity.

Wavelength dispersive electron microprobe analyses were acquired using a JEOL-733 electron microprobe equipped with Advanced Microbeam automation. The accelerating voltage was 15 kV, the beam current was nominally 30 nA, and the beam diameter was 1 μm, except that a 10 μm diameter beam was utilized for one spot each on the Py_{100} and Mj_{80} samples. Silicates and oxides were used as primary standards; the La standard was the rare-earth glass described in Drake and Weill (1972). X-ray matrix corrections were based on a modified Armstrong (1988) CITZAF routine incorporated into the software. Some totals were slightly low, 98% (Table 3), attributable to imperfect polish.

Of our four samples, only Mj_{39} (Table 3) is chemically inhomogeneous, ranging from Mj_{26} to Mj_{50} among its large grains, which are several to 10 μm across. The surface contains about 8% voids, due to plucked grains. Less than 10% of the sample consists of sub-micrometer-sized interstitial matter, discussed further by Giesting et al. (in preparation). Because the interstitial grains are too small to reflect the IR light coherently (scattering occurs) and are volumetrically insignificant, the effect on the IR spectra is only a loss of intensity. Their small size and low volume also prohibit identification through X-ray diffraction. The large garnet grains of Mj_{39} were examined in the Raman microprobe measurements, but the specific composition for the ~1 μm-sized spot that was probed is unknown. The remaining samples are chemically homogeneous with grain sizes below 10 μm, such that Mj_{80} is texturally the most homogenous and has the smallest grains with sizes below 2 μm.

TABLE 3. Electron microprobe analyses (in oxide wt%)

Sample no.	G729	2720S			2988	2722S
Composition	Py_{100}	min.	Mj_{39}(ave)*	max.	Mj_{45}	Mj_{80}
MgO	29.28(27)	32.12	33.69(87)	34.21	34.99(28)	37.57(42)
Al_2O_3	24.90(47)	18.61	15.4(14)	12.41	14.22(25)	4.63(53)
SiO_2	45.06(35)	49.13	50.87(87)	51.92	48.92(14)	56.37(60)
FeO	0.15(13)	0.08	0.03(4)	bld	0.00(3)	0.03(3)
Cr_2O_3	0.03(3)	n.a.	0.09(12)‡	n.a.	0.04(4)	0.1(2)
La_2O_3	0.11(13)	n.a.	bld ‡	n.a.	0.03(3)	0.09(17)
Total	99.53	99.9	100.0	98.5	98.2	98.7
No. spots analyzed	6†	1	19‡	1	2	5
Ave Mj (mol%)	0	26	39	50	45	80

Notes: Values in parentheses are standard deviations; n.a. = not analyzed; bld = below the limit of detection. Detection limits at 95% confidence for the trace oxides in wt % are: FeO = 0.12; Cr_2O_3 = 0.14; La_2O_3 = 0.25. Ti, Zr, Ni, and Ca were below the limits of detection. Majorite contents were determined from each of Al, Si and Mg wt %, and averaged: uncertainties are ±1.

* The Mj_{39} sample is inhomogeneous. The matrix varies as shown and also contains <10% interstitial material. For details on impurities, see Giesting et al. (in prep).

† One additional anomalous spot was found during analysis of pyrope, which was deficient in silicon and enhanced in aluminum and magnesium.

‡ Cr and La were measured for two spots only.

Majorites synthesized in the same manner for a different study were found to be single-phase garnets, on the basis of ultrasonic experiments and X-ray diffraction (see, e.g., Gwanmesia et al. 2000). Because our microprobe analyses showed that three of our four samples are homogeneous on a micrometer-scale, and since all our results are consistent with a garnet-like structure and composition, it was unnecessary to perform additional XRD measurements.

Single-crystal, natural pyrope from Dora Maira (Chopin 1984; sample number GTF3 in Hofmeister et al. 1996), provided by G.R. Rossman, served as a spectral standard. The chemical composition is $Py_{94}Al_4Gr_2$, where Al = $Fe_3Al_2Si_3O_{12}$ and Gr = $Ca_3Al_2Si_3O_{12}$.

Spectroscopic methods

Infrared spectra were obtained at ambient conditions using an evacuated Bomem DA3.02 Fourier transform interferometer (FTIR) using a SiC globar as the source. Mid-IR data (4000–500 cm^{-1}) utilized a liquid N_2 cooled HgCdTe detector and a KBr beamsplitter. Far-IR acquisitions used a liquid He cooled silicon bolometer and either a 3 μm coated Mylar beam-splitter for 600 to 100 cm^{-1} or a 12 μm plain Mylar below 100 cm^{-1}. Between 1000 and 1500 scans were collected at a resolution of 1 cm^{-1}.

Reflectance IR spectra were collected using a Spectratech FTIR microscope. Merging was done by scaling the far-IR spectra to match the mid-IR spectra in the 500–600 cm^{-1} region. For the Mj_{39} sample, the lowest spectral range (υ < 100 cm^{-1}) was added in the same manner. Because no peaks were detected below 100 cm^{-1}, this range was neglected for the other samples. Kramers-Kronig analyses (e.g., Spitzer et al. 1962) were performed on merged spectra (~100 to 4500 cm^{-1}) that were scaled to account for the loss of light due to scattering. For pyrope, the scaling factor (x1.61) was determined by comparing the reflectivity (R) of the polycrystalline sample to R of natural, single-crystal pyrope (Fig. 1a). For the other samples, the maximum value of R was assumed to be 92%, as determined for natural pyrope, and the raw spectra were scaled by about 1.3, as indicated in the figures to follow. For Kramers-Kronig analysis, R was assumed to be constant at frequencies below the range of measurements. The resulting dielectric and optical functions are not always reasonably behaved near 100 cm^{-1} so we cut off the reported functions at 150 to 180 cm^{-1} (e.g., Fig. 1b). For higher frequencies, we tried both Wooten's (1972) approximation, and also assumed that R is constant, but found little difference in the dielectric functions. We report the dielectric functions obtained assuming constant R at high υ for the polycrystals because this approach minimizes the effect of frequency-dependent scattering known to occur at high υ. Peak positions of the transverse optic (TO) modes and full widths at half maximum (FWHM) were obtained from the peaks in the real part of the dielectric function (ε_2) and are reported below. Longitudinal optic (LO) positions were obtained from the minima in the imaginary part of ($1/\varepsilon$). For details regarding analysis of reflectivity data, see Hofmeister (1995) and Hofmeister et al. (1996).

Mid- and far-IR absorption spectra were collected from thin films made by compressing a few grains in a Mao-Bell diamond anvil cell (DAC), and by using a beam condenser to interface the DAC with the spectrometer. The grains were obtained by scraping a small area of the sample (see Hofmeister and Mao 2001 for details).

Raman spectra were obtained with a laser Raman microprobe. The device is a fiber-optically coupled microscope-spectrometer-detector system from Kaiser Optical Systems, Inc. The Nd-YAG frequency-doubled laser emits at 532 nm (18,797 cm^{-1}) with a maximum output of 100 mW. The system consists of an f/1.8 holographic imaging spectrograph, a 2048-channel CCD array detector, and a Leica polarized-light microscope. The samples were analyzed in the 180° backscattering configuration; the spot size was ~1 μm. Spectra were taken from the same spot with both scrambled (unpolarized) and polarized incident light such that the two polarizations are at right angles. Our polarized Raman experiments, however, will neither reveal all the symmetries (e.g., Table 1), nor all the modes, because the exact orientation of the microscopic crystals with respect to that of the polarizer is unknown. For the same reason, we did not polarize the scattered light because no additional information would have been gained. The intent of our experiments was to explore whether any modes are polarized, and if different responses are seen for the various samples.

The peak fitting routines in Grams/AE versions 6 and 7 were used to obtain peak parameters for the dielectric functions and Raman spectra. Lorentzian peak

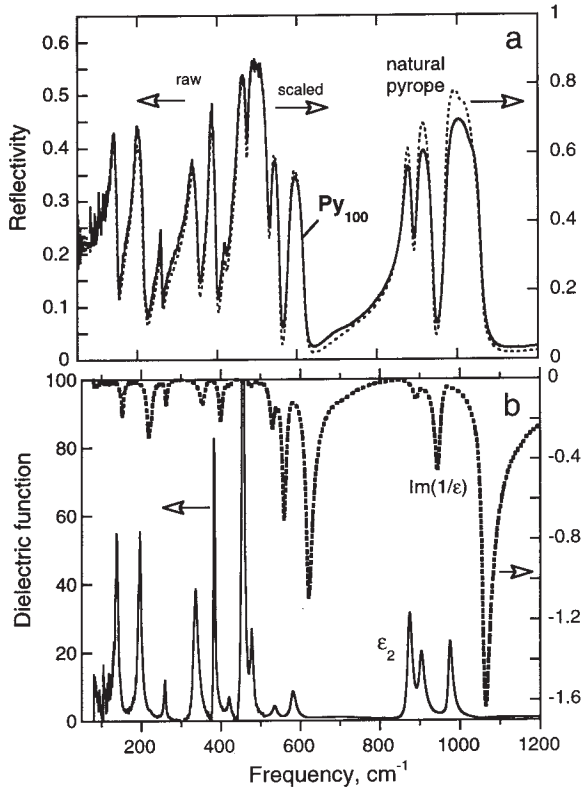

FIGURE 1. IR reflectance spectrum of Py_{100} and the dielectric functions derived from Kramers-Kronig analysis. (**a**) Reflectivity. Dotted line and right y-axis = single-crystal pyrope (GTF3 from Hofmeister et al. 1996). Solid line and left y-axis = raw reflectivity for Py_{100}. The scale factor of $x1.61$ used for Kramers-Kronig analysis was obtained by comparing the left and right y-axes. (**b**) The dielectric functions ε_2 (solid line, scale on left side) and im(1/ ε) (broken line, scale on right side).

shapes were used, and these are theoretically expected (e.g., Burns 1990). Only rarely were peaks needed in addition to the obvious shoulders and well-resolved peaks to achieve a reasonable residual. The questionable peaks are indicated in the tabulated data. Some peaks were only resolved in the polarized data, and their widths are not reported. Peak-fitting routines cannot be used to deconvolute absorption spectra of lattice modes because the peak shapes are neither Lorentzian, nor Gaussian, nor a combination (e.g., Wooten 1972; Hofmeister 1995).

SPECTROSCOPIC DATA AND BAND ASSIGNMENTS

Infrared-active lattice modes

The IR-reflectance spectra of the Al-rich majorites (Figs. 2 and 3) resemble published reflectivity spectra of cubic garnets, especially Fe-poor pyropes (Fig. 1, see also Hofmeister and Chopelas 1991; Hofmeister et al. 1996). More peaks exist in the reflectivity spectrum of Mj_{80} (Fig. 4). Weak peaks at the same positions as the extra, symmetry-breaking peaks in Mj_{80} are also seen in the dielectric functions of Mj_{39} and Mj_{45}. Figure 5 provides examples. Many of the peaks in Mj_{45} are unresolved multiplets. Except for a few isolated modes, e.g., near 700 cm^{-1}, the peaks of Mj_{39} carry over to Mj_{45}, as shown in Table 4.

Most peak positions for pyrope can be traced across the binary (Table 4), only υ_2 at 455 cm^{-1} and υ_3 at 871 cm^{-1} are not found in Mj_{80}. All three majorites have peaks that are not found

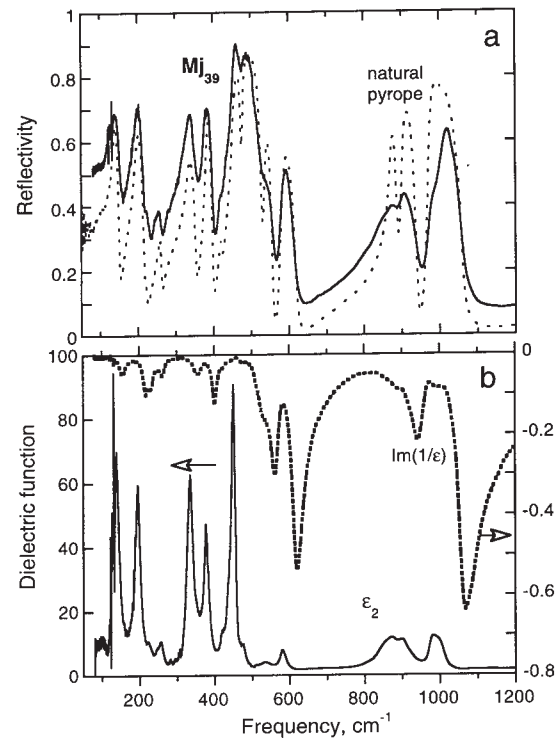

FIGURE 2. Reflectivity and derived functions for Mj_{39}. The raw spectrum was scaled by $x1.34$ for Kramers-Kronig analysis. See Fig. 1 for description.

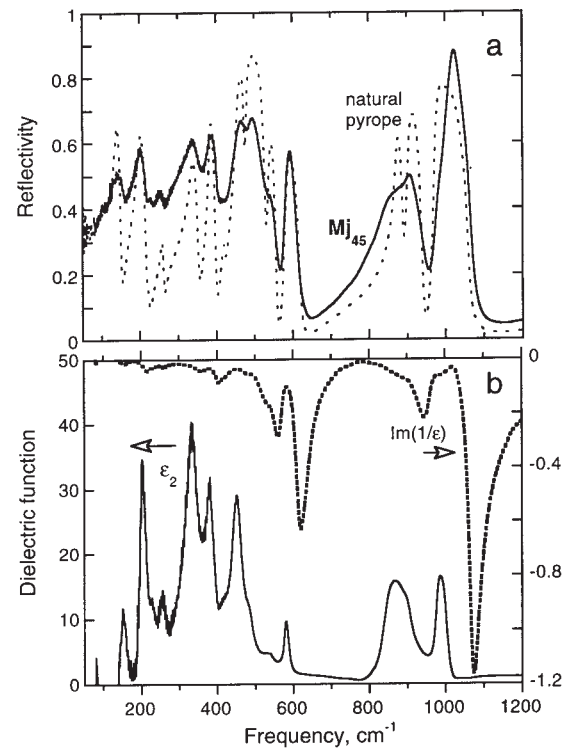

FIGURE 3. Reflectivity and derived functions for Mj_{45}. The raw spectrum was scaled by $x1.29$ for Kramers-Kronig analysis. See Fig. 1 for description.

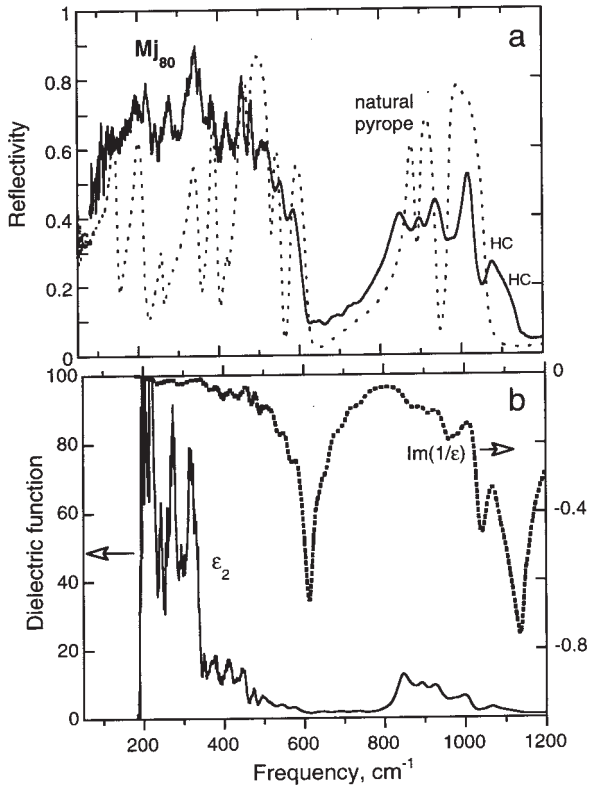

FIGURE 4. Reflectivity and derived functions for Mj_{80}. The raw spectrum was scaled by $x1.38$ for Kramers-Kronig analysis. See Fig. 1 for description. Note the huge number of peaks. HC = hydrocarbon impurities.

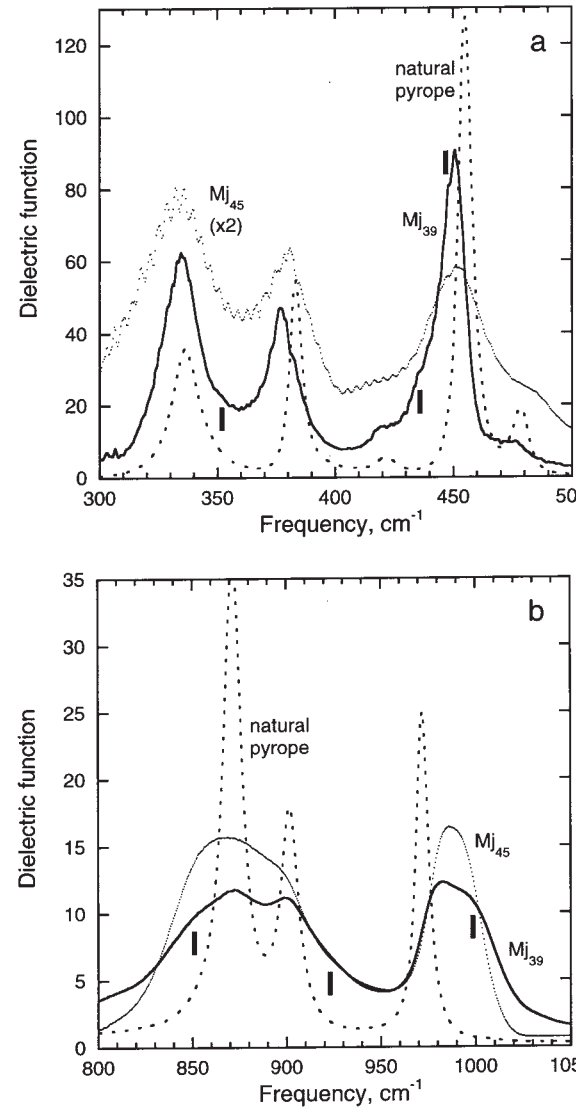

FIGURE 5. Expanded view of ε_2. (**a**) O-Si-O bending region. (**b**) Si-O stretching region. Finely dotted curve = single-crystal pyrope. Solid line = Mj_{39}. Heavy dots = Mj_{45}. Vertical bars mark the shoulders seen in Mj_{39} not expected for cubic garnets. A break in slope near 928 cm^{-1} suggests that a peak probably exists in Mj_{39}, as in Mj_{80}.

in pyrope, with positions independent of the Mj content (Table 4). More "symmetry breaking" peaks are resolved in Mj_{39} than in Mj_{45}, partially because the peak widths are narrower (on average) in Mj_{39} (Table 4). Peaks between ~600 and 700 cm^{-1} are not present in Mj_{45}. As peaks in this area are relatively narrow, isolated from the remaining modes, and located in the flat and transparent segment of the spectrum between the bending and stretching modes, they would not have been obscured by broadening. One new peak appears in Mj_{45} at 492 cm^{-1}. All of the extra peaks in Mj_{39} and Mj_{45} also exist in Mj_{80}, but Mj_{80} has ~10 additional peaks, e.g., 722 and 928 cm^{-1}. Peak widths in Mj_{80} resemble those of Mj_{39}, leaving Mj_{45}, which is close to the mid-point of the binary, with the widest peaks (Table 4). Similar compositional dependences of the FWHM, owing to dodecahedral and octahedral cation disorder, are seen in IR reflectivity data for pyrope-almandine ($Fe_3Al_2Si_3O_{12}$) and grossular-andradite ($Ca_3Al_2Si_3O_{12}$-$Ca_3Fe_2Si_3O_{12}$) garnets, respectively (Giesting and Hofmeister 2002).

To gauge the accuracy of the Kramers-Kronig analysis, the absorption coefficients calculated from reflectivity data are compared to measurements of IR absorbance from the thin films (Fig. 6). The absorption coefficient is related to reflectivity through

$$A(\upsilon) = 4\pi\upsilon\, k(\upsilon) = 4\pi\upsilon\, \varepsilon_2(\upsilon)/n(\upsilon) \quad (1)$$

where $n + ik$ is the complex index of refraction, and ε_2 is the imaginary part of the dielectric function (e.g., Wooten 1972; Hofmeister 1995). In deriving Equation 1, light is assumed to attenuate exponentially with distance. Comparing A to absorbance from spectral measurements requires correction for surface reflections or scattering, and allowing for the use of common (not the natural) logarithm in spectral analysis packages and in mineralogical studies. Thus,

$$Ad = 2.3026\,[a_{chem} + 2\log(1\text{-}R)] \quad (2)$$

where d is thickness, R is reflectivity, $a_{chem} = -\log(I_{tra}/I_0)$ is the measured "chemical" absorbance, and I is the intensity, transmitted or incident to the sample. For the thin film measurements of silicates, the reflectivity of the diamonds dominates, but this

effect is eliminated when absorbance is calculated from the ratio of the raw sample spectrum (I_{tra}) to the reference spectrum of the empty DAC (I_0). The measurements are affected by the presence of interference fringes due to parallel diamond faces in the transparent spectral region above ~1000 cm^{-1} (Figs. 6a and 6d), but these artifacts are easily separated from the lattice modes.

The thin-film spectra are in good agreement with the calculated absorption coefficients (Fig. 6). The peak positions are virtually identical, the widths are closely reproduced, and relative intensities are reasonably similar. Peak positions from the thin films (Table 5) are higher than the TO frequencies (Table 4) because the presence of the LO component in absorbance measurements skews the peak toward higher frequencies. This effect is implicit in Equation 1 wherein ε_2, which has Lorentzian peak shapes, is divided by the index of refraction, which has a derivative shape. The only obvious differences between the measurements and calculations are that (1) the LO components are exaggerated in the thin-film data, due to non-normal incidence in the DAC and also because *R* in Equation 2 was neglected, and (2) some additional peaks are seen in the thin film data. These consist of two types of peaks, overtone-combination bands or hydrocarbon impurities (Fig. 6). The weak and very broad peaks seen in the thin-film spectra in the fairly transparent regions between the O-Si-O bending and Si-O stretching modes (υ from 650 to 800 cm^{-1}), and above the Si-O stretching region ($\upsilon > 1100$ cm^{-1}), are not fringes, but are probably overtones. The signal-to-noise ratio is better in the thin-film spectra than in reflectance, probably because scattering was eliminated by compression. Both Py_{100} and Mj_{45} show these patterns.

For Mj_{80}, reflectivity is high in the far-IR relative to the mid-IR region (Fig. 4), as indicated by the comparison of calculated *A* to measured absorbance (Fig 6d). As this sample has a relatively fine and homogenous grain-size, the problem is likely caused by secondary reflections from within the grains, which adds to the specular reflectivity of the surface. Reflectivity is excessive in the far-IR because the far-IR absorptions are weaker, allowing some photons to reach the back surface of the uppermost grains. The other samples have large enough grains (several micrometers across), such that reflections from the back-surfaces do not affect the spectra.

Despite the above problem, our thin-film data for Mj_{80} resemble previous mid-IR measurements of Mj_{100} obtained from dispersions of powder in KBr pellets (Jeanloz 1981; Kato and Kumazawa 1985; McMillan et al. 1989). The peak positions differ significantly for the lowest Si-O stretching mode, which is attributed to rounding of peaks in the dispersion due to some particles being too large to transmit at all frequencies (see Hofmeister 1995; Hofmeister et al. in review). Many of the weaker peaks found here for Mj_{80} were not detected in Mj_{100}, which could be due to the limitations of the KBr method. Our thin-

TABLE 4. Peak parameters (in cm^{-1}) from Kramers-Kronig analysis of the IR reflectance spectra

Cubic	Pyrope§		Py_{100}		Mj_{39}		Mj_{45}		Mj_{80}		Tetrag.
assign.	υ	FWHM	υ	FWHM	υ	FWHM	υ	FWHM	υ	FWHM	assign.
T,T_{dod}	136.3	9.3	138	10.3	137	21	152†	9.0	?	?	$T,T_{Mg,dod}$
T_{dod}	194.9	12.1	196	9.8	194	18.6	203	15.3	204	13.6	$T_{Mg,dod}$
T_{dod}	222.7	6.1	~220		225	13	225	24	220	9	$T_{Mg,dod}$
									228	10	
									243	9.4	$T_{Mg,dod}$
T_{oct}	259.0	7.2	259	5	254	24	255	27	259	10.4	T_{oct}
									274	18.3	?
					~290	~16			296	17.5	T_{oct}
									318	20.3	?
T,R	336.7	13.7	337	12.7	335	19.2	333	53*	332	10.2	R
					356	20.6			349	14.9	R
R	383.4	6.0	384	4.4	378	15.5	380	20	374	27.6	R
T_{oct}	421.0	5.9	420	4.8	419	14.0	~410	~10	411	23.0	T_{oct}
					439	17.6			432	9.1	T_{oct}?
					448	9.3			446	13.8	T_{oct}?
υ_2	455.2	6.6	456	7.5	452	7.5	452	33	–	–	υ_2
T_{oct}	478.4	6.4	478	8.7	476	11.0	484	27	473	9.2	T_{oct}
							492	10	496	9.2	υ_2
									510	24.0	υ_4
υ_4	535.2	10.6	535	14	532	62*	535	53*	544	26.7	υ_4
υ_4	581.5	13.0	582	15	581	19	581	22	576	27.3	υ_4
									634	18.2	υ_4
υ_4	~650								650	21.7	υ_4
					679	15			682	20.5	Si_{oct}-O-Si_{tet}
			700*	106*	695	19	~700*	weak	696	12.8	Si_{oct}-O-Si_{tet}
	~750*						~750*	weak	722	11.3	Si_{oct}-O-Si_{tet}
					841	43	847	23	846	39.6	$\upsilon_1(E_u)$
υ_3	871.3	12.2	875	12.4	867	62*	863	31	~860	weak	υ_3
υ_3	901.6	11.0	904	17.0	903	39.4	899	54*	890	49.3*	υ_3
							~920?	weak	928	38.2	$\upsilon_1(A_u)$
υ_3	972.0	7.7	976	12.9	981	20.7	988	25	977	40.7*	υ_3
					999	24.0	992	weak	1000	24‡	(υ_3)
Avg.1	N=14	9.4	N=14	10.3	N=22	23.2	N=16	27.3	N=29	20.0	
Avg.2					N=20	19.4	N=13	21.3	N=27	18.1	

Notes: For symbols, see Table 1. T denotes the translation of the SiO_4 tetrahedron.
* Overtone-combination modes. Weak indicates this feature is too weak to constrain the FWHM.
† Probably the 137 cm^{-1} mode was obscured by noise and the 152 cm^{-1} is a symmetry breaking mode, as both were seen in Mj_{80} absorbance, Table 5.
‡ Mj_{80} has a series of strong reflectances at 1067, 1100, 1275, 1540, and 1730 cm^{-1}, attributed to hydrocarbons, discussed by Giesting (2002) and Giesting et al. (in prep.).
§ Natural single-crystal pyrope from Dora Maira, sample GTF3 from Hofmeister et al. (1996).

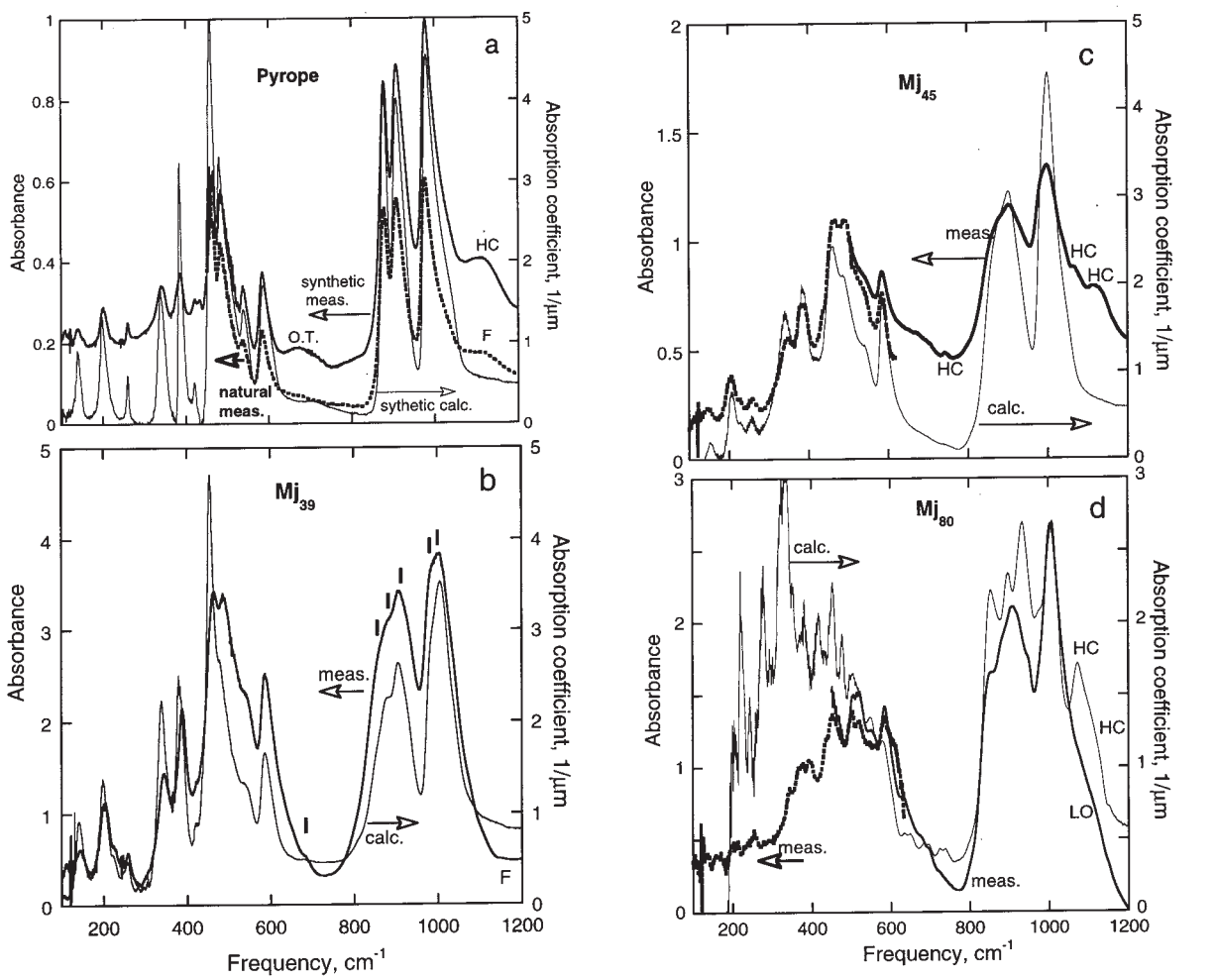

FIGURE 6. Comparison of measured "meas." and calculated "calc." absorption spectra of the lattice modes. Heavy solid and dotted lines, left y-axis = IR thin film absorbance spectra, using natural logarithm units. Thin lines, right y-axis = absorption coefficient calculated from Kramers-Kronig analysis. (**a**) Py_{100}. Dots = mid-IR thin-film of natural pyrope. HC = hydrocarbon contaminants. F = interference fringes. O.T. = overtones. From the comparison, the pyrope films have thickness of about 0.2 μm. (**b**) Mj_{39}. Thickness ~1 μm. (**c**) Mj_{45}. Thickness ~0.4 μm. (**d**) Mj_{80}. Thickness ~1 μm for the mid-IR film. The far-IR absorbance (dots) was scaled by *x*2 to match the mid-IR.

film data for the Al-rich majorites resemble mid-IR data from dispersions (McMillan et al. 1989), but a mismatch again exists between the lowest frequency υ_3 modes, which is attributed to sampling technique. For Al-rich compositions, the IR modes of cubic garnet dominate. The weak modes, which are known to be interspersed among the strong modes in Si-rich majorites, are difficult to resolve in IR spectra of dispersions of the Si-rich majorites, and are not seen at all in dispersion spectra of Al-rich majorites.

A series of peaks between 1040 to 1860 cm^{-1}, likely to be hydrocarbons, occurs intermittently in both the thin film data and in reflectance spectra (Table 5 footnotes). These and other impurities are discussed in detail by Giesting et al. (in preparation).

The good agreement shown in Figure 6 indicates that the Kramers-Kronig analysis, after scaling *R*, is accurate for these polycrystalline samples, and that the parameters in Tables 4 and 5 reasonably represent the majorite-pyrope binary. Because the IR data are unpolarized, the results mainly depict the doubly degenerate E_u symmetry. Peak assignments (Table 4) were made with this in mind, and by using Tables 1 and 2. In assigning peaks, less attention is paid to the IR data for Mj_{100} from McMillan et al. (1989) because the KBr method can induce artifacts and commonly provides excess LO contributions. Mode assignments for peaks traceable across the binary are straightforward. Assignments for some symmetry breaking peaks (such as Si-O tetrahedral stretches and translations of Mg in the distorted dodecahedron) are obvious due to the peak locations. However, mode mixing is likely to be present for frequencies between 300 and 500 cm^{-1}, where many modes overlap. Therefore, mode assignments for some bands in the tetragonal phases are uncertain. The sharp peaks near 700 cm^{-1} are assigned as Si_{oct}-O-Si_{tet} bends. Bands at 840 and 922 cm^{-1} are assigned as υ_1, because this type of mode occurs in the IR of olivine or in the Raman spectra of garnets. No clear evidence exists of Si-octahedral stretching in the IR spectra. Note that the translations of the octahedral cations at 259, 421, and 478 cm^{-1} carry across the binary, despite the

TABLE 5. Peak positions (in cm^{-1}) from thin-film absorbance spectra

Assign.	Pyrope*	Py_{100}	Mj_{39}	Mj_{45}	Mj_{80}	Mj_{100}†
T			111	~112?	106?	
					125	
T,T_{dod}	144*	137	143	146	137	
(T_{dod})					159	
			183	183?	173?	
T_{dod}	204*	200	202	203	198	
					213	
T_{dod}	220*	222 sh	225	228	228?	
(T_{dod})			245		246	
T_{oct}	260*	260	258	255	256	
(T_{oct})			282 sh		290	
?			302	302,314?	317 sh	
T,R	343*	340	343	345	344	354?M
(R?)					367	362?M
(R?)			373	380	377	383M
R	389*	386	388	387	395	398
T_{oct}	421*	421	421	422		416M
(T_{oct}?)				436?	436	446
					452	
υ_2	460	462	463	462	468sh	
T_{oct}	483	485	486	489		490M
LO or (υ_2)					503	501
υ_4			514	515?	515	521
υ_4	537	539	540	544	550	549
υ_4	584	584	583	583	584	580
LO					604?	604
(υ_4)			632		633	627K
(υ_4)			652		652	650J
(Si_{oct}-O-Si_{tet})			682	674?	680	675
(Si_{oct}-O-Si_{tet})					698	693
(Si_{oct}-O-Si_{tet})				743‡	725	
(υ_1)			857	~855	852	827
υ_3	877.5	878	878	878	881	879
υ_3	907.8	908	905	903	909	906
(υ_1)					922sh	
(υ_3)				~935	949	954
υ_3	977	977	979	985	975sh	
(υ_3)			1000	999	1004	1000

Notes: Peak positions are barycenters obtained by inspecting the traces. Assignments in parentheses refer to tetragonal garnets. Shoulders considered to be LO modes and overtone-combinations in the cubic spectra are omitted. One spectrum of Py_{100} also has hydrocarbon contamination peaks at 1041, 1067s, 1120s, 1263s, 1287, 1370, 1402, 1450, 1490, 1542, 1581, 1600, 1725s, 1742, and 1860 cm^{-1}, where s indicates a strong peak. Similar, but weaker patterns of peaks are seen in some spectra of Mj_{39}, Mj_{45}, and Mj_{80}. These, hydroxyl, and water are discussed by Giesting et al. (in prep.). Artifacts are seen at 110 and 120 cm^{-1} in some samples, LO mode is at 610 cm^{-1} in many.

* McAloon and Hofmeister (1993), on pyrope synthesized by Haselton and Westrum (1980). Mid-IR thin film spectra acquired from Dora Maira pyrope, see Hofmeister et al. (1996) for details.

† Previous data from KBr dispersions, which have stronger contributions from LO components than the thin-film measurements presented here. Peaks marked M are only seen by McMillan et al. (1989). Peaks marked K were seen only by Kato and Kumazawa (1985). Peaks marked J were seen only by Jeanloz (1981). Unlabeled peaks were reported by more than one of these sources.

‡ Probably due to a hydrocarbon impurity.

change in charge: clearly mass effects dominate octahedral and dodecahedral translations. This assignment is supported by the absence of such positions from in the Raman spectra of either pyrope or majorite (see below), as expected from symmetry analyses (Tables 1 and 2).

The IR spectra of the Al-rich samples differ from that of pyrope by having additional Si-O stretching modes at 841–847 cm^{-1} and 992-1000 cm^{-1}, and from that of Mj_{80} by the Si-O stretch of cubic garnet near 860–870 cm^{-1} being strong, and by lacking the Si-O stretch at 928 cm^{-1} (Table 4). The ~860 cm^{-1} band in Mj_{80} is suggested by the large residual from peak fitting, but because fits including such a peak are ambiguous, parameters for this feature are not included in Table 4. Overlapping peaks are also present in the O-Si-O bending region, whereas the low frequency region contains weak, well-resolved peaks.

The Si-O-Si bending modes (Table 5) follow the pattern of 675–682, 693–698, and sometimes 722 cm^{-1}, in our samples as well as in Mj_{100} (McMillan et al. 1989), which differs substantially from patterns of Si_{tet}-O-Si_{tet} bends seen in ortho-, clino-, and aluminous enstatites. The pyroxenes have frequencies of 649–653, 681–700, 736–757, and either 725 (ortho or clino) or 770 (Al-rich) cm^{-1} (Keppel, Hofmeister, and Bowey, unpublished data; see also Farmer 1974). Reversion of garnet to pyroxene or impurities can be ruled out, and the modes from 650 to 750 cm^{-1} in majorite garnets are due to Si_{oct}-O-Si_{tet} bending. Generally, these modes occur for compositions of ~Mj_{25} and ~Mj_{75} where octahedral-tetrahedral coupling due to the imbalance in bonding around the Si tetrahedron should be greatest, and are thus compatible with the existence of two-mode behavior, as discussed above. The appearance of Si_{oct}-O-Si_{tet} bending modes in Mj_{100}, at first glance, does not perfectly agree with our analysis of the majorite structure. However, the Si_{oct}-O-Si_{tet} bending modes observed for Mj_{100} in the Raman spectrum of McMillan et al. (1989) were not seen by Rauch et al. (1996), Manghnani et al. (1998), or Chopelas (1999). Samples of Mj_{100} are known to have partial Mg,Si ordering at the octahedral sites (e.g., Angel et al. 1989; Phillips et al. 1992). The amount of disorder appears to crucially affect octahedral-tetrahedral coupling, given that Mj_{39} (with small FWHMs and thus some order) has these local modes, whereas Mj_{45} (with large FWHMs and thus disorder) does not. We suggest that the sample of McMillan et al. (1989) is either disordered, or has a small amount of impurities such as Cr^{3+} or OH^- (see Giesting 2002; Giesting et al. in preparation) that could cause truncation of the Si-Si-Si- chains.

In summary, our IR results are consistent with the structural transitions and space groups of aluminous majorites proposed by Nakatsuka et al. (1999a) based on crystallographic refinements. Substantially more modes are seen for Mj_{80} than for Mj_{39} or Mj_{45}, and the types of modes seen in the Al-rich majorites agree with symmetry analysis (Table 1).

Raman-active lattice modes

The polarized data have a lower signal-to-noise ratio than the unpolarized measurements, due to reduced throughput, and thus do not reveal the weakest modes. We take this difference into account in comparing the measurements.

The unpolarized Raman spectra of polycrystalline and single-crystal pyrope (Fig. 7a) differ slightly from the two polarized spectra, consistent with cubic symmetry and random orientation of the crystals. Only the T_{2g} species are affected by polarization (Table 6), and the changes are slight (Fig. 7a). The peak widths and positions (Table 6) are similar for natural and synthetic pyrope: slight differences in the FWHM are probably due to the uncertainties in the spectral fits or to orientational differences because the average FWHM are the same.

The Raman spectra of the three majorites (Fig. 7b–d) are more affected by polarization, some peaks strongly so. This behavior indicates a lower symmetry than cubic. Because Mj_{80} is tetragonal, this result confirms that the Al-rich majorites are also non-cubic. That the Al-rich majorites have fewer modes than Mj_{80} with the $I4_1/a$ structure suggests the $I4_1/acd$ space group. The spectrum of Mj_{45} appears to be a broadened version of the

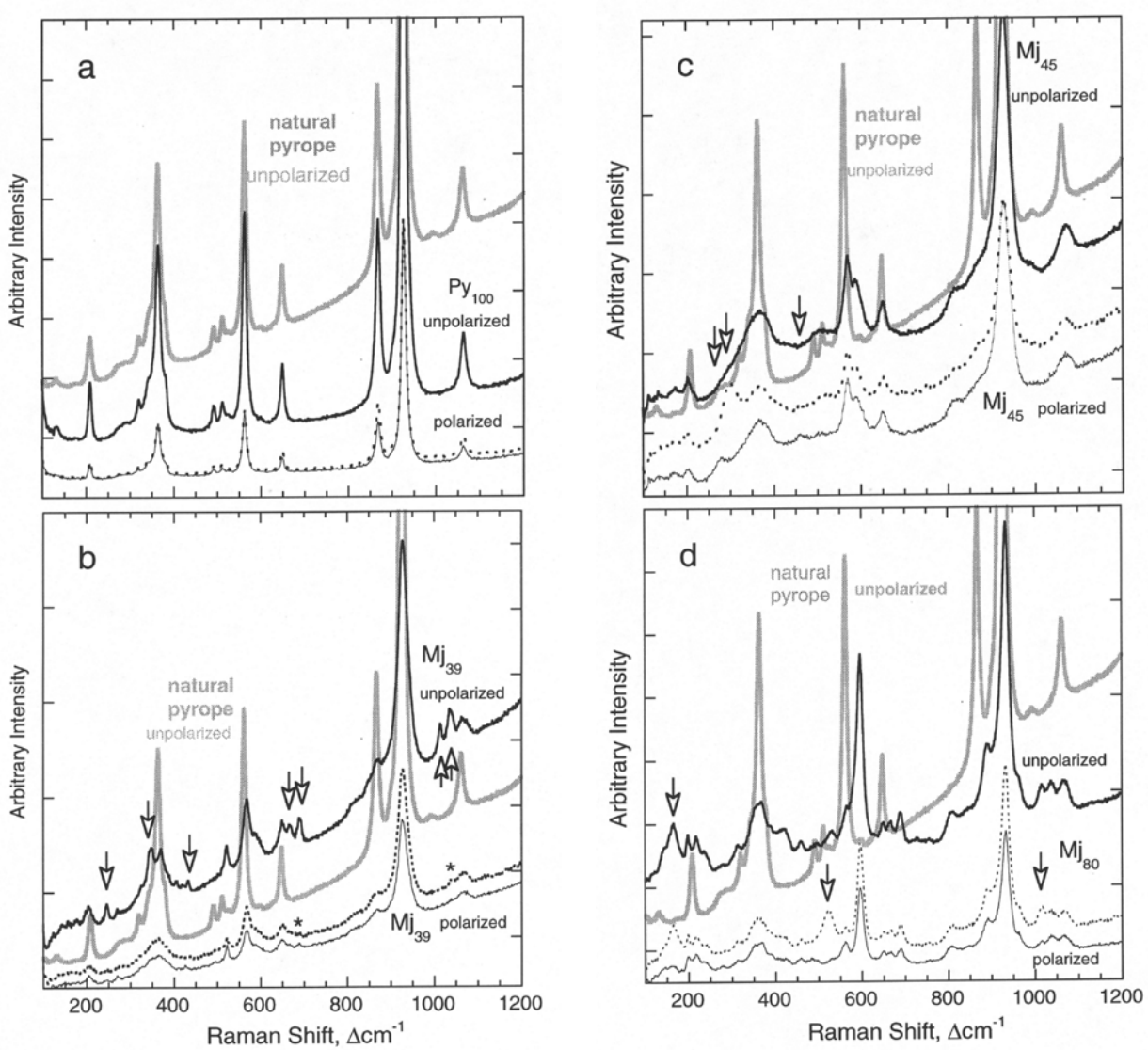

FIGURE 7. Raman spectra of the lattice modes. (**a**) Py_{100}. (**b**) Mj_{39}. (**c**) Mj_{45}. (**d**) Mj_{80}. Raw data, uncorrected for background or fluorescence are shown. In each section, thick black curve = unpolarized data of the sample. Thin black and dotted curves = polarized data on same spot as the unpolarized measurement. Thick grey = unpolarized spectrum of single-crystal pyrope. Arrows indicate strongly polarized peaks. Asterisks mark weak expressions of these peaks in the polarized spectra.

Mj_{39} spectrum, although peaks exist in Mj_{39} that should have been resolved in Mj_{45}, but were not, e.g., in the Si-O-Si bending region (Table 6). Polarized measurements revealed some peaks in Mj_{45} that were not resolved in the unpolarized spectrum (Table 6). The Mj_{80} sample has more peaks than either of the Al-rich majorites, with an average FWHM between the two.

Our spectra from Mj_{45} closely resemble previous measurements near the middle of the binary (McMillan et al. 1989; Manghnani et al. 1998). For the Mj_{39} sample, more peaks are resolved and they have narrower widths. Given the heterogeneity of Mj_{39}, and the compositions encountered in electron microprobe analysis (Table 3), it is likely that the actual μm-sized grain probed in the Raman measurements differs from the average composition (see the discussion). Our Raman spectra for Mj_{80} closely resemble results for Mj_{93} by Rauch et al. (1996), but diverge from previous data for Mj_{80} in Manghnani et al. (1998). Except for the modes involving octahedral Si, our data are much like Manghnani et al's. (1998) spectrum of Mj_{100}, which is considerably broader than that of McMillan et al. (1989). NMR data from the Mj_{80} sample of Manghnani et al. (1998) indicates almost complete cation disorder (Phillips et al. 1992). Clearly, the differences among the Raman spectra for samples with nominally the same compositions are related to varying degrees of cation ordering, because such ordering is temperature dependent and the various samples were synthesized along different pressure-temperature paths and at different conditions.

The compositional dependence of the FWHM and the appearance of symmetry-breaking peaks in the Raman spectra roughly

TABLE 6. Peak positions and widths (in cm^{-1}) from unpolarized Raman spectra

	Ia$\bar{3}$*d*			*I*4$_1$/*acd*					*I*4$_1$/*a*				
Cubic Assign.	Pyrope n	Xtl FWHM	Polyxtl. FWHM	Mj_{39} υ	FWHM	Mj_{45} υ	FWHM	A_{1g}**	Mj_{80} υ	FWHM	Mj_{93}† υ	Mj_{100}† υ	A_g**
				~122		~114	w		~115				
T-T_{2g} §	131	8	~12	143	~10	135	~10		142	~17		136‡	T
				157	~10				165	28 sp			
T-E_g #	~175	~15	~10	176.7	9.7	173.4	24.7	T	~183	p			T
T_{dod}-E_g,T_{2g}	208.0d	10.2	7.7	203.7	18.0	203.3	14.3	T_{dod}	199	10	197	196,200	$2T_{dod}$
									218	19	220	222	
				245.8	9.1 sp				239	18	237	234,255	
T_{dod}-T_{2g}	271.2	15.7	-	269.8	5.3	277	p		280	32	273	273	T_{dod}
O.T.-T_{2g} §	290.9	30.0*	37.4*			299	sp						
T-T_{2g}	318.9	11.4	10.5	321.7	27.5	314	92*		312.3	17.7	303	308	T
											332&	332	
T-T_{2g},E_g #	342.5	21.7	23.9	346.8	20.1 sp				354.8	37.8* p		355	T
R-A_{1g},E_g	363.4d	14.0	14.9	369.9	22.0	364	86*	2R	369.9	15.7	363&	366	2R
R-T_{2g}	379.5	8.1	7.7	387.0	14.2				390.4	48.8*	388		R
				405.6	9.6 p						395&	397	
				420.5	8.8 p				421.1	28.3 p			
υ$_2$-E_g	(439)			432.5	5.5 sp	437	83*	$υ_2$				428	$υ_2$
						458	p		459.6	13.3	454&	456	$υ_2$?
υ$_2$-T_{2g}	490.6	9.3	9.5 p	495	p	491	p		493.0	37.6 p		493	$υ_2$
υ$_4$-T_{2g}	511.0	8.7	10.0 p	510	p	504	82*	$υ_2$,mix				516	$υ_4$
υ$_2$-E_g	524.6	15.0	10.2	520.9	10.7 p				521,531	21.9 sp	528	533	$υ_2$
υ$_2$-A_{1g}	561.6	10.9	11.3	567.4	18.0	568.6	18.5	$υ_2$	568.8	39.7*		554	$υ_2$
									583	p			
υ$_4$-T_{2g}	598.9	3.3	3.9	590.7	22.8	591	31	$υ_4$	596.2	17.2	593	599	$υ_4$
υ$_4$-E_g #	(626)§												
υ$_4$-T_{2g}	647.7	9.1	9.6	649.4	16.1	650	20.5		648.5	12.0	645	647	$υ_4$
				667.5	14.0 sp			Si_{oct}-O-Si_{tet}	665.9	15.0	660&		Si_{oct}-O-Si_{tet}
				690.0	9.7 sp			Si_{oct}-O-Si_{tet}	689.7	20.8	684&		Si_{oct}-O-Si_{tet}
				816.0	39.8	816	52		806.7	26.7	793	800	
				846.9	8.9				842.0	63*		852	
υ$_3$-T_{2g}	867.0	12.5	12.9 p	867.8	36.7	865	50						
υ$_3$-T_{2g}	899.4	5.2	3.8			892	43		889.5	28.7	889	885	$υ_3$
υ$_1$-E_g	(911)								919.4 ||	31 ||			
υ$_1$-A_{1g}	925.5	11.9	12.3	927.8	26.6	929	33	2υ$_1$, υ$_3$	933.2	19.2	927	930	2υ$_1$, υ$_3$
υ$_3$-E_g	(938)												
									964.9	10.7	Sh	964	$υ_3$
						993 ||	10 ||		990	p			
				1013.9	7.5 sp	1015?		Si_{tet}-Si_{oct}	1015.4	18.7 p			Si_{tet}-Si_{oct}
				1037.0	16.0 sp			Si_{tet}-Si_{oct}	1038.0	23.2 p			Si_{tet}-Si_{oct}
υ$_3$-T_{2g}	1061.4	15.7	15.2	1066.9	28.6	1070	44		1068.0	23.7		1065	$υ_3$
Avg.1	*N*=19	12.4	12.4	*N*=26	16.3	*N*=16	43		*N*=28	24.8	~11	~5	
Avg.2	*N*=18	11.4	10.9	*N*=24	14.5	*N*=12	29		*N*=24	21.1			

Notes: The Raman spectra are acquired in units of Δcm^{-1}. For comparison to IR data, we assume that the modes frequencies (in cm^{-1}) are equivalent to the measurements. Averages of the FWHM are given at the bottom, with the number (*N*) of peaks used. For pyrope, frequencies in parenthesis are from Hofmeister and Chopelas (1991). Assignments to T_{1g} are from Kolesov and Geiger (1998; 2000). Peaks marked d are doublets resolved in these earlier polarized measurements. Peak positions listed without widths were detected in the polarized spectra. Sh = shoulder; sp = strongly polarized; p = polarized.

* Peak not used in Avg.2, bottom line, because these bands consist of several poorly resolved peaks

† Rauch et al. (1996). "Typical" FWHM are reported. Data for Mj_{93} are between ~170 and ~1000 cm^{-1}; Mj_{100} extends to higher υ. Peaks that merge in pairs at 59 kbar are marked by "&".

‡ Chopelas (1999). Her other peaks are similar to those reported by Rauch et al. (1996).

§ The 130 cm^{-1} mode of pyrope was confirmed to be two modes at low temperature (Kolesov and Geiger 2000). This coincides with both IR (Fig. 2) and acoustic modes. The 290 cm^{-1} mode, which is very broad, is an overtone (acoustic modes), not a fundamental in T_{1g} as assigned by Hofmeister and Chopelas (1991), see Kolesov and Geiger 2000).

The E_g modes of pyrope are very weak and overlap with A_{1g} and T_{2g} peaks. All available spectra (Hofmeister and Chopelas 1991; Kolesov and Geiger 1998, 2000) have some contributions from the other polarizations. Because the 626 cm^{-1} peak in pyrope is not seen for any other samples, this is probably an overtone. The peak at 342 cm^{-1} is probably T_{2g} symmetry. We observe a weak peak at 175 cm^{-1} that extends across the series and is instead assigned to T in E_g for pyrope. The low frequency is consistent with the assignment.

|| This peak is poorly resolved and may be an artifact.

** For the tetragonal majorites, mode assignments are given for the A-type modes only. Also listed are motions connected with octahedral Si that arise from local modes (two-mode behavior), see text.

follow the behavior of the IR peaks. The Raman spectra are more complicated, probably because individual, micrometer-sized grains were sampled, and the spectra depend partially on crystallographic orientation. For the IR method, sampling over most of the surface removes polarization differences by averaging. Also, two polarizations exist for IR-active modes, whereas three symmetries occur for Raman-active modes of cubic garnets, and four symmetries exist for the tetragonal space groups (Tables 1, 2). Nonetheless, the appearance of symmetry-breaking peaks in the Raman spectra are compatible with the space groups proposed by Nakatsuka et al. (1999a). The most compelling evidence for assigning *I*4$_1$/*acd* as the space group of Mj_{39} and Mj_{45} is that both E_g and A_{1g} modes of pyrope exist in their unpolarized spectra, in accord with Table 1. In contrast, for Mj_{80} and the even more Si-rich majorites of Rauch et al. (1996), all the modes of pyrope are found in the unpolarized spectra, in accord with the *I*4$_1$/*a* space

group (Table 2). Note that the considerable broadening of the Mj_{45} sample means that many peaks exist, but are not resolved, as can be seen by comparing the polarized and unpolarized spectra (Fig. 7c) as well as the peak positions (Table 6).

The occurrence of Si_{oct}-O-Si_{tet} modes for Mj_{39} and Mj_{80}, but not for Py_{100}, Mj_{45}, or for Mj_{100} of Rauch et al. (1996), also repeats the patterns in the IR. Pyroxene spectra differ, with orthopyroxenes having a doublet at 660-670 cm^{-1}, whereas clinopyroxenes have one band near in this spectral region (see Wang et al. 2001), thus excluding reversion as a possible source of these bending modes. The associated modes at 1015 and 1038 cm^{-1} are assigned to stretches involving octahedral Si (Table 6). Because these are related to the symmetric stretch of the tetrahedron, these peaks should be strong in Raman spectra. Their presence in Raman, but not IR spectra, is consistent with this assignment. Their appearance in spectra of solid solutions, but not at the midpoint of the binary or for the end-members, is further consistent with assignment to local modes.

Peak parameters vs. composition

Raman and IR peak positions for members of the pyrope-majorite series are relatively independent of composition (Fig. 8), unlike those in other garnet series (e.g., McAloon and Hofmeister 1995; Hofmeister et al. 1996). Both the infrared and Raman peaks shift by an amount smaller than ~10 cm^{-1} across the binary (Tables 4–6). Some changes are associated with the appearance of symmetry-breaking modes. The observation of roughly constant peak positions is consistent with the lattice constant changing little across the binary (Nakatsuka et al. 1999a) and with the similar atomic masses of the substituting cations (Mg, Al, and Si). Because observation of two-mode behavior requires non-overlapping peaks (Chang and Mitra 1968), the two-mode behavior connected with other octahedral substitutions in garnet (McAloon and Hofmeister 1995) should not occur for this series. The Si_{oct}-O-Si_{tet} bending and Si_{tet}-Si_{oct} stretching peaks exist as local modes, as these have no counterpart in pyrope.

Peak widths increase dramatically toward the middle of the binary (Fig. 9), as observed in other garnet series (Giesting and Hofmeister 2002). For the Raman modes, the peaks that could be traced across the series all behave similarly. However, FWHMs of the Si-O stretching motions increase more than those of the bending motions (Fig. 9a). For the IR modes, similar behavior is seen, and in addition some of the bending motions and rotations-librations of the tetrahedra are also strongly affected (Fig. 9b).

The mean width of the Raman modes in the inhomogeneous sample Mj_{39} is decidedly lower than that of the IR modes, whereas for the other samples, the Raman widths are greater than those derived from IR data. Thus, we infer that the spot from which the Raman data were obtained must correspond to one of the Al-rich grains. An Al content as low as Mj_{26} is possible (Table 3), although the distribution seen in electron microprobe analyses indicates that Mj_{36} is the most probable composition for the spot examined with Raman spectroscopy.

Discussion

The changes in the IR and Raman spectra are attributed to changes in space group across the series and to the presence of new modes arising from two-mode behavior. Other materials, such as $K(Mg,Cu)F_3$ perovskites, behave similarly (Burns et al. 1996), but the type of two-mode behavior seen in majoritic garnets is at present unique. The behavior of garnets is intrinsically complicated by the large number of vibrational modes, but the peak positions being nearly independent of composition in this series aids in interpretation. Thus, two-mode behavior can be distinguished from phase transition effects by the modes crossing the compositional ranges of the different structures, i.e., Si_{oct}-O-Si_{tet} bending is seen in ~Mj_{39}, Mj_{80}, Mj_{93} (of Rauch

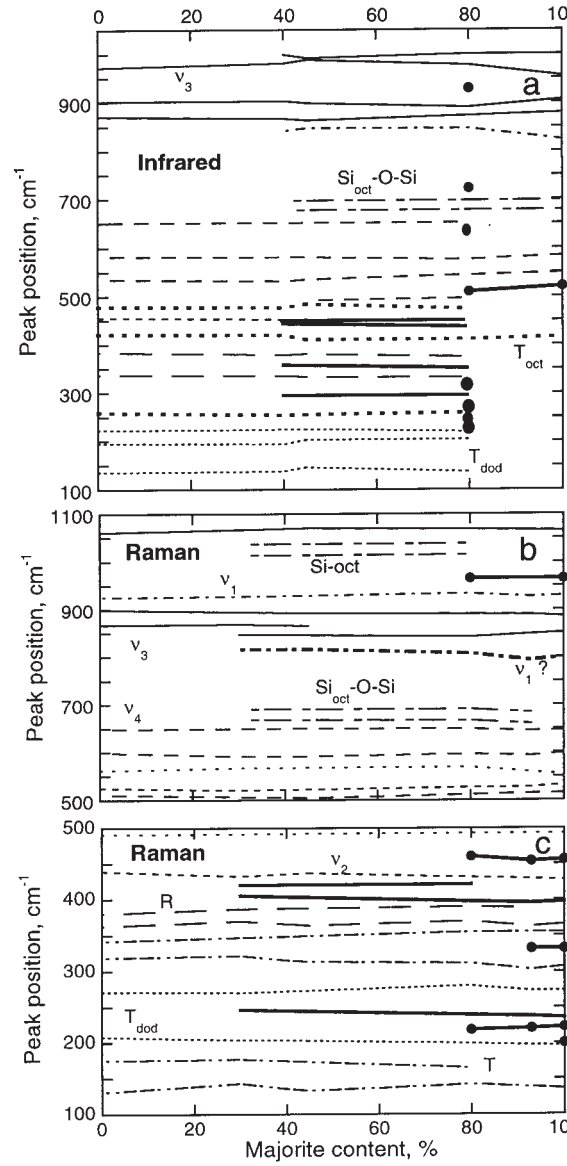

Figure 8. Dependence of frequency on composition. (**a**) IR reflectivity data with absorption positions for Mj_{100} from McMillan et al. (1989). (**b**) Raman modes at high frequency. Mj_{93} and Mj_{100} data from Rauch et al. (1996). (**c**) Raman modes at low frequency. Dots = positions found only for > 80% Mj. Thick lines = assignment unclear. Various types of lines = modes as assigned in Tables 4 and 6. The number of modes increases discontinuously with majorite content such that jumps occur at Mj_{39} and Mj_{80}

et al. 1996) and sometimes in Mj_{100} (of McMillan et al. 1989). Cation disorder, however, seems also to obliterate the Si_{oct}-O-Si_{tet} bending mode as it is not observed in the disordered Mj_{80} of Manghnani et al. (1998), nor in Mj_{45} in the present study. Because disorder broadens peaks, it may be that these very low-intensity peaks exist in Mj_{80} of Manghnani et al. (1998), but cannot be distinguished from spectral noise.

For the pyrope-majorite series, the increase in the number of modes is compatible with the $I4_1/acd$ space group for Al-rich majorites, and with $I4_1/a$ for Si-rich majorites. The simplest spectrum observed (for Mj_{45}) has too many peaks for the cubic structure, even if the extra peaks due to two-mode behavior are excluded from this count. In addition, strong polarization of some of the Raman modes are seen for the binary samples, but not for the cubic garnets near Py_{100}. Even though the types of modes seen in the Raman spectra agree with the $I4_1/a$ space group assigned to Si-rich majorites, this deduction is not conclusive because the same behavior (all the Raman modes in cubic garnet are folded into the A-type symmetries) occurs for other space groups (see theory section). However, given that several crystallographic refinements of end-member majorite confirm $I4_1/a$ (e.g., Angel et al. 1989; Heinemann et al. 1997), it is unnecessary to consider other possibilities. For the Al-rich majorites, the presence of E_g modes from the cubic phase in their unpolarized spectra exclusively implicates the $I4_1/acd$ space group. These same E_g modes are overwhelmed by the activation of the T_{2g} modes in the spectra of $I4_1/a$ majorites. Our results thus corroborate the refinements of Nakatsuka et al. (1999a), which showed a change in volume between Mj_{24} and Mj_{38}, and interpreted this as evidence of the $I4_1/acd$ space group for the mid-section of the binary. Our results corroborate Nakatsuka et al's. (1999a) compositional limit of cubic garnets (Si-rich pyropes) as being near Mj_{30}.

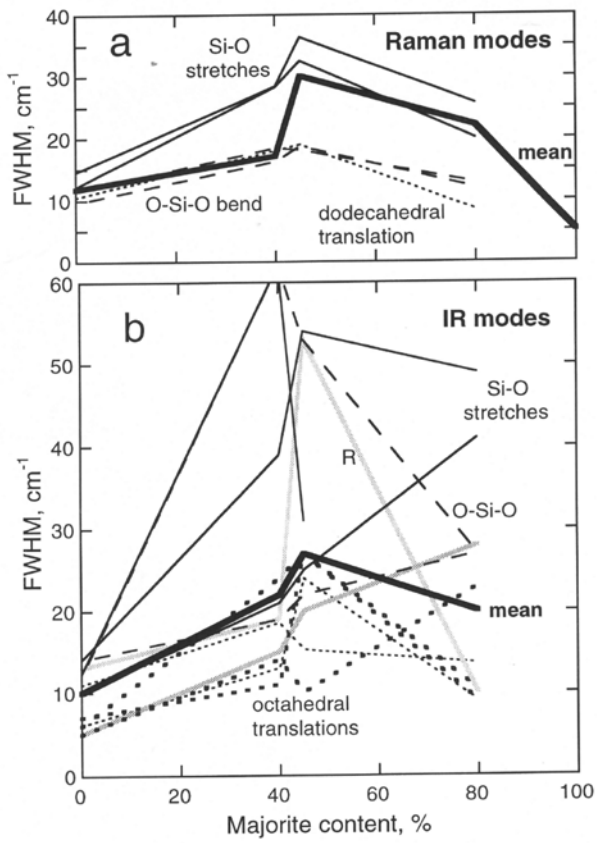

.**FIGURE 9.** Dependence of FWHM on composition. (**a**) Unpolarized Raman data. Mj_{93} and Mj_{100} data from Rauch et al. (1996). (**b**) IR reflectivity data. Modes that could be traced across the boundary are shown. Modes that were unresolved multiplets were excluded.

Rauch et al. (1996) observed that for Mj_{93} near 59 kbar, the modes at 660 cm^{-1} associated with Si_{oct}-O-Si_{tet} bending disappear upon compression, whereas the mode at 683 cm^{-1} intensifies. At this pressure, two pairs of peaks (335, 363 cm^{-1} and 395, 454 cm^{-1}) merge. The peaks that disappear in the merging are not A_g symmetry (Table 6) and the changes are reversible, suggesting accidental degeneracy. In contrast, the Mj_{100} peaks remain resolvable at high pressure. This difference is consistent with peak widths for Mj_{100} being about half those of Mj_{93}. However, as Rauch et al. (1996) noted, the high-pressure spectra of Mj_{93} have a pattern similar to that of the Al-rich majorites. An alternative interpretation is that the various Y sites in $I4_1/a$ become indistinguishable, and that a transformation to $I4_1/acd$ occurs at high pressure. Transformation to the cubic structure can be ruled out, based on the large number of peaks. Hatch and Ghose (1989) dismissed transitions between these space groups, which cannot be correct because $I4_1/a$ is a subgroup of $I4_1/acd$ (see Fateley et al. 1972 and the discussion of Nakasutka et al. 1999a). Transformation would proceed via a different mechanism than that envisioned by Hatch and Griffin (1989).

Because the $I4_1/acd$ structure has only one octahedral site, adoption of this structure above ~Mj_{30} obviously does not involve ordering of Mg, Si, or Al. Nakatsuka et al. (1999a) discuss changes in electron density and polarization effects as the driving force for reduced symmetry at intermediate compositions. If the octahedral site was ordered for Al-rich majorites, then the sorting would involve not two, but rather three, sites. In this regard, the large amount of Al stabilizes the single octahedron in the structure. That changes in electron density inferred by Nakatsuka et al. (1999a) do exist across the series is corroborated by the appearance of bands associated with Si_{oct}-O-Si_{tet} bending motions. The spectral pattern differs from that of pyroxenes, but the existence of a low intensity, narrow series of bands from 650 to 750 cm^{-1} certainly results from a bridging O atom in a chain. The frequencies in majorites and enstatite-rich pyroxenes are similar because it is mainly the mass of the Si atom that controls the frequency. Vibrational modes are mainly derived from nearest-neighbor interactions, and thus, the bonding of the two types of Si atom (tetrahedral or octahedral) to their respective nearest neighbors is a secondary effect.

The IR spectrum of Mj_{18} measured by McMillan et al. (1989) is compatible with the $I4_1/acd$ space group. In contrast, the sample of Mj_{24} examined by Nakatsuka et al. (1999a) appears to be cubic. As partial cation ordering is known (e.g., Angel et al. 1989), the compositional phase boundaries may be "fluid," depending on such factors as cooling history and impurities, which influence cation ordering. For example, a sample of 34% Mj-18% Py-14% $Mg_3Cr_2Si_3O_{12}$ has the $I4_1/a$ space group (Nakatsuka et al. 1999b), whereas binary samples require greater than 75% Mj to be $I4_1/a$ (Heinemann et al. 1997), and the Mj_{80} sample

examined by Manghnani et al. (1998) has a Raman spectrum suggesting that its structure is $I4_1/acd$, not $I4_1/a$. A possible explanation of these contradictory results is that hydroxyl impurities are sometimes present, and that this entity affects ordering by enhancing diffusion rates. In addition, the different approaches to synthesis may promote or retard cation ordering. For example, Nakatsuka et al. (1999a) used PbO fluxes, but Heinemann et al. (1997), who concluded that garnets below 75% Mj are cubic, did not. The variation in peak widths from similar compositions supports variable amounts of order at a given chemical composition. Given the above results, subtle disagreements among elasticity measurements along the binary (cf. Gwanmesia et al. 2000; Sinogeikin et al. 1997) likely originate from samples having different structures and/or disorder, despite the fact that the compositions were similar.

The observation of different spectra for samples with subtle structural differences means that vibrational spectra of garnets are sensitive to (1) the content of the dodecahedral site, and (2) ordering at the octahedral site. Infrared spectra of natural, birefringent garnets (McAloon and Hofmeister 1993; Hofmeister et al. 1996) do not have the distinctive changes seen here for majorite-pyrope garnets. Because many aluminous garnets have wavy extinction (e.g., Hofmeister et al. 1998), strain probably causes birefringence in the $(Ca,Fe,Mg,Mn)_3Al_2Si_3O_{12}$ quaternary. For the $Ca_3(Al,Fe,Cr)_2Si_3O_{12}$ ternary, it may be worthwhile considering the effect of substitution of Al for Fe^{3+} on electrostatic interactions as a possible explanation of strong birefringence.

Under mantle conditions, majorite garnet should be stable in the cubic structure according to symmetry analysis of twinning present in the end-member (Hatch and Ghose 1989). However, this analysis considered cation ordering, not the less obvious symmetry-reducing transitions considered here, as the driving force, and thus it is possible that the $I4_1/acd$ structure discovered for samples near the middle of the Mj-Py binary by Nakatsuka et al. (1999a), and confirmed in the present work, is actually the stable phase at mantle conditions. Differentiating the $I4_1/acd$ space group from the cubic parent probably requires spectroscopic measurements at elevated pressures and temperatures in conjunction with crystallographic studies, as the unit cells examined so far are metrically cubic.

The presence of three different structures, disorder, and changes in bonding across the binary has thermodynamic implications. If the three garnet-type structures encountered for majorite have the same types of vibrational modes (i.e., octahedral-tetrahedral coupling is not present), then only the activities of the modes change among the structures (Tables 1 and 2). For this case, the thermodynamic properties are not affected by the particular space group (Giesting et al. 2004). Although the presence of Si_{oct}-O-Si_{tet} and Si_{tet}-Si_{oct} modes (Tables 3–6) alters heat capacity and entropy, and configurational entropy also exists, these changes are small (Giesting et al. 2004). The composition expected for the mantle is roughly Mj_{75}, at which the maximum number of bridging O atoms is expected, and thus maximum cation disorder pertains. The thermodynamic properties and phase relations in the mantle are obviously dependent on the specific chemical composition and structure of majorite, but the results of the present study can be used to provide a reasonable representation of mantle garnet (Giesting et al. 2004).

ACKNOWLEDGMENTS

Syntheses were performed in the Stony Brook High Pressure laboratory, which is jointly supported by the State University of New York at Stony Brook and the NSF Science and Technology Center for High Pressure Research (EAR 89-20239). The synthesis was also supported by research grants to R.C. Liebermann (EAR 93-0450 and 96-14612) and G.D. Gwanmesia (EAR-0106528). Support for P.A.G. and A.M.H. was provided by NSF-EAR-0125883 and 0207198. We thank G.R. Rossman for providing the natural pyrope, and H. Keppler and an anonymous reviewer for constructive criticism.

REFERENCES CITED

Akaogi, M. and Akimoto, S. (1977) Pyroxene-garnet solid solution equilibria in the systems $Mg_4Si_4O_{12}$-$Mg_3Al_2Si_3O_{12}$ and at high pressures and temperatures. Physics of the Earth and Planetary Interiors, 15, 90–106.

Angel, R.J., Finger, L.W., Hazen, R.M., Kanzaki, M., Weidner, D.J., Liebermann, R.C., and Veblen, D.R. (1989) Structure and twinning of single-crystal $MgSiO_3$ garnet synthesized at 17 GPa and 1800°C. American Mineralogist, 74, 509–512.

Armstrong, J.T. (1988) Quantitative analysis of silicate and oxide minerals: comparison of Monte-Carlo, ZAF, and Phi-Rho-Z procedures. In D.E. Newbury, Ed., Microbeam Analysis, 239–246. San Francisco Press, California.

Bass, J.D. Anderson, D.L. (1984) Composition of the upper mantle: geophysical test of two petrological models. Geophysical Researh Letters, 11, 229–232.

Burns, G. (1990) Solid State Physics, 810 pp. Academic Press, San Diego.

Burns, P., Hawthorne, F.C., Hofmeister, A.M., and Moret, S.L. (1996) A ferroelastic phase transition in $K(Mg_{1-x}Cu_x)F_3$ perovskite. Physics and Chemistry of Minerals, 23, 141–150.

Chang, I. F. and Mitra, S. S. (1968) Application of a modified long-range isodisplacement model to long-wavelength optic phonons of mixed crystals. Physical Review, 172, 924–933.

Chopelas, A. (1999) Estimates of mantle relevant Clapeyron slopes in the $MgSiO_3$ system from high-pressure spectroscopic data. American Mineralogist, 84, 233–244.

Chopin, C. (1984) Coesite and pure pyrope in high-grade blueshists of the Western Alps: a first record and some consequences. Contributions to Mineralogy and Petrology, 86, 107–118.

Drake, M.J. and Weill, D.F. (1972) New rare earth element standards for electron microprobe analysis. Chemical Geology, 10, 179–181.

Farmer, V.C. (1974) The Infrared Spectra of Minerals. Mineralogical Society, London.

Fateley, W.G., Dollish, F.R., McDevitt, N.T., and Bentley, F.F. (1972) Infrared and Raman selection rules for molecular and lattice vibrations: The correlation method, 222 pp. Wiley Interscience.

Gasparik, T. (1989) Transformation of enstatite-diopside-jadeite pyroxenes to garnet. Contributions to Mineralogy and Petrology, 102, 389–405.

——— (1990) Phase relations in the transition zone. Journal of Geophysical Research, 95, 15751–15769.

Giesting, P.A. (2000) Spectroscopy and Thermal Conductivity of Mantle Garnets. M.A. Thesis, Washington University, St. Louis.

Giesting, P.A. and Hofmeister, A.M. (2002) Thermal conductivity of disordered garnets from infrared spectroscopy. Physical Review B, 65, paper 144305, 16 p.

Giesting, P.A., Hofmeister, A.M., Wopenka, B., Gwanmesia, G.D., and Jolliff, B.L. (2004) Thermal conductivity and thermodynamic properites of majorite: implications for the transition zone. Earth and Planetary Science Letters, in press.

Gwanmesia, G.D. and Liebermann, R.C. (1992) Polycrystals of high pressure phases of mantle minerals: hot-pressing and characterization of physical properties. In Y. Syono and M.H. Manghnani, Eds., High-Pressure Research: Application to the Earth and planetary Sciences, 117–135. Terrapub, Tokyo/American Geophysical Union, Washington, D.C.

Gwanmesia, G.D., Liebermann, R.C., and Guyot, F. (1990) Hot-pressing and characterization of polycrystals of β-Mg_2SiO_4 for acoustic velocity measurements. Geophysical Research Letters, 17, 1331–1334.

Gwanmesia, G.D., Li, B., and Liebermann, R.C. (1993) Hot pressing of high pressure phases of mineral phases of mantle minerals in multi anvil apparatus. Pure and Applied Geophysics, 141, 467–484.

Gwanmesia, G.D., Liu, J., Chen, G., Kesson, S., Rigden, S.M., and Liebermann, R.C. (2000) Elasticity of the pyrope ($Mg_3Al_2Si_3O_{12}$)–majorite ($Mg_4Si_4O_{12}$) garnets solid solution, Physics and Chemistry of Minerals, 27, 445–452.

Haselton, H.T. Jr. and Westrum, E.F. Jr. (1980) Low-temperature heat capacities of synthetic pyrope, grossular, and $pyrope_{60}$-$grossular_{40}$. Geochimica et Cosmochimica Acta, 44, 701–709.

Hatch, D.M. and Ghose, S. (1989) Symmetry analysis of the phase transition and twinning in $MgSiO_3$ garnet: implications to mantle mineralogy. American Mineralogist, 74, 1221–1224.

Hatch, D.M. and Griffin, D.T. (1989) Phase transitions in grandite garnets. American Mineralogist, 74, 151–159.

Heinemann, S., Sharp, T.G., Seifert, F., and Rubie, D.C. (1997) The cubic-tetragonal

phase transition in the system majorite ($Mg_4Si_4O_{12}$)–pyrope ($Mg_3Al_2Si_3O_{12}$). Physics and Chemistry of Minerals, 24, 206–221.

Hirose, K., Yagi, T., Funakoshi, K.-I., Fei, Y., and Ono, S. (2001) In situ measurements of the phase transition boundary in $Mg_3Al_2Si_3O_{12}$. Earth and Planetary Science Letters, 184, 567–573.

Hofmeister, A.M. (1995) Infrared microscopy in the Earth Sciences. In H. Humicki, Ed., Practical Guide to Infrared Microspectroscopy, 377–416. Marcel Dekker Inc., New York.

Hofmeister, A.M. and Chopelas, A. (1991) Vibrational spectroscopy of end-member silicate garnets. Physics and Chemistry of Minerals, 17, 503–526.

Hofmeister, A.M. and Mao, H.K. (2001) Evaluation of shear moduli and other properties of silicates with the spinel structure from IR spectroscopy. American Mineralogist, 86, 622–639.

Hofmeister, A.M., Fagan, T.J., Campbell, K.M., and Schaal, R.B. (1996) Single-crystal IR spectroscopy of pyrope-almandines with minor amounts of Mn and Ca. American Mineralogist, 81, 418–428.

Hofmeister, A.M., Schall, R.B., Campbell, K.M., Berry, S.L., and Fagan, T.J. (1998) Prevalence and origin of birefringence in 48 garnets form the pyrope-almandine-grossular-spessartine quarternary. American Mineralogist, 83, 1293–1301.

Horak, M. and Vitek, A. (1978) Interpretation and Processing of Vibrational Spectra. Wiley, New York.

Irifune, T. and Ringwood, A.E. (1987) Phase transformations in primitive MORB and pyrolite compositions to 25 GPa and some geophysical implications. In M.H. Manghnani and Y. Syono, Eds., High Pressure Reseach in Mineral Physics, 231–242. Terra Scientific, Tokyo.

Jeanloz, R. (1981) Majorite: vibrational and compressional properties of a high-pressure phase. Journal of Geophysical Research, 86, 6171–6179.

Kanzaki, M. (1987) Ultrahigh-pressure Phase relations in the system $Mg_4Si_4O_{12}$-$Mg_3Al_2Si_3O_{12}$. Physics of the Earth and Planetary Interiors, 49, 168–175.

Kato, T. and Kumazawa, M. (1985) Garnet phase of $MgSiO_3$ filling the pyroxene-ilmenite gap at very high temperature. Nature, 316, 803–805.

Kolesov, B.A. and Geiger, C.A. (1998) Raman spectra of silicate garnets. Physics and Chemistry of Minerals, 25, 142–151.

——— (2000) Low-temperature single-crystal Raman spectrum of pyrope. Physics and Chemistry of Minerals, 27, 645–649.

Manghnani, M.H., Vijayakumar, V., and Bass, J.D. (1998) High-pressure Raman scattering study of majorite-garnet solid solutions in the system $Mg_4Si_4O_{12}$-$Mg_3Al_2Si_3O_{12}$. In M.H. Manghnani and T. Yagi, Eds., Properties of Earth and Planetary Materials at High Pressure and Temperature, 129–137. American Geophysical Union, Washington, D.C.

McAloon, B.P. and Hofmeister, A.M. (1993) Symmetry of birefringent garnets from infrared spectroscopy. American Mineralogist, 78, 957–967.

———(1995) Single-crystal IR spectroscopy of the grossular-andradite binary. American Mineralogist, 80, 1145–1156.

McMillan, P., Akaogi, M., Ohtani, E., Williams, Q., Nieman, R., and Sato, R. (1989) Cation disorder in garnets along the $Mg_3Al_2Si_3O_{12}$-$Mg_4Si_4O_{12}$ join: an infrared, Raman, and NMR study. Physics and Chemistry of Minerals, 16, 428–435.

Nakatsuka, A., Yoshiasa, A., Yamanaka, T., Ohtaka, O., Katsura, T., and Ito, E. (1999a) Symmetry change of majorite solid-solution in the system $Mg_3Al_2Si_3O_{12}$-$MgSiO_3$. American Mineralogist, 94, 1135–1143.

Nakatsuka, A., Yoshiasa, A., Yamanaka, T., and Ito, E. (1999b) Structure refinement of a birefringent Cr-bearing majorite $Mg_3(Mgj_{0.34}Si_{0.34}Al_{0.18}Cr_{0.14})_2Si_3O_{12}$. American Mineralogist, 94, 199–202.

Phillips, B.L., Howell, D.A., Kirkpatrick, R.J., and Gasparik, T. (1992) Investicaton of cation order in MgSiO3-rich garnet using ^{29}Si and ^{27}Al MAS NMR spectroscopy. American Mineralogist, 77, 704–712.

Rauch, M., Keppler, H., Häfner, W., Poe, B., and Wokaun, A. (1996) A pressure-induced transition in $MgSiO_3$-rich garnet revealed by Raman spectroscopy. American Mineralogist, 81, 1289–1292.

Ringwood, A.E. and Major, A. (1966) High-pressure transformations in pyroxenes. Earth and Planetary Science Letters, 1, 351–357.

Sawamoto, H. (1987) Phase diagram of $MgSiO_3$ at pressures up to 24 GPa and temperatures up to 2200 ∞C: phase stability and properties of tetragonal garnet. In M.H. Manghani and Y. Syono, Eds., High-pressure Research in Mineral Physics, 209–219. American Geophysical Union, Washington, D.C.

Sinogeikin, S., Bass, J.D., O'Neill, B., and Gasparik, T. (1997) Elasticty of tetragonal end-member majorite and solid solution in the system $Mg_4Si_4O_{12}$-$Mg_3Al_2Si_3O_{12}$. Physics and Chemistry of Minerals, 24, 115–121.

Spitzer, W.G., Miller, R.C., Kleinman, D.A., and Howarth, L.W. (1962) Far-infrared dielectric dispersion in $BaTiO_3$, $SrTiO_3$, and TiO_2. Physical Review, 126, 1710–1721.

Vacher, P., Moquet, A., and Sotin, C. (1998) Computation of seismic profiles from mineral physics; the importance of the non-olivine components for explaining the 660 km depth discontinuity. Physics of the Earth and Planetary Interiors, 106, 275–298.

Wang, A., Jolliff, B.L., Haskin, L.A., Kuebler, K.E., and Viskupic, K.M. (2001) Characterization and comparison of structural and compositional features of planetary quadrilateral pyroxenes by Raman spectroscopy. American Mineralogist, 86, 790–806.

Weidner, D.J. and Wang, Y. (2000) Phase transformations; implications for mantle structure. In Earth's deep interior; mineral physics and tomography from the atomic to the global scale: Geophysical Monograph 117, 215–235.

Wooten, F. (1972) Optical properties of solids. Academic Press, San Diego.

MANUSCRIPT RECEIVED NOVEMBER 11, 2002
MANUSCRIPT ACCEPTED JUNE 18, 2003
MANUSCRIPT HANDLED BY LEE GROAT